Serafin Knitel, BSc

Defect Analysis of Abrasive Wear of Cutting Inserts

MASTER THESIS

For obtaining the academic degree
Diplom-Ingenieur

Master Programme of
Technical Physics

Graz University of Technology

Supervisor:

Ao.Univ.-Prof. Dipl.-Ing. Dr.techn. Werner Grogger

Co-Supervisor:

Dipl.-Ing. Dr.techn. Evelin Fisslthaler

Institute for Electron Microscopy and Nanoanalysis

Graz, February 2013

Deutsche Fassung:
Beschluss der Curricula-Kommission für Bachelor-, Master- und Diplomstudien vom 10.11.2008
Genehmigung des Senates am 1.12.2008

EIDESSTATTLICHE ERKLÄRUNG

Ich erkläre an Eides statt, dass ich die vorliegende Arbeit selbstständig verfasst, andere als die angegebenen Quellen/Hilfsmittel nicht benutzt, und die den benutzten Quellen wörtlich und inhaltlich entnommene Stellen als solche kenntlich gemacht habe.

Graz, am ……. ……..
(Unterschrift)

Englische Fassung:

STATUTORY DECLARATION

I declare that I have authored this thesis independently, that I have not used other than the declared sources / resources, and that I have explicitly marked all material which has been quoted either literally or by content from the used sources.

……. ……..
date (signature)

Abstract

Indexable inserts are nowadays non-replaceable tools in machining metals and they are composed of hard carbide particles and a soft metallic binder. Mostly tungsten carbide which is embedded in cobalt as a binder is used. These compositions are called cemented carbides. Especially the excellent wear resistance of cemented carbides makes them interesting for machining. In their field of work indexable inserts should be reliable and accurate. Accuracy is achieved by surface treatments like grinding. However, during operation it can be observed that ground cemented carbides may possess a shorter life time than unprocessed cemented carbides.

An overview about the known wear mechanism in tungsten carbide, cobalt and in compound of these is given. Surface investigations of ground and unprocessed cemented carbides starting with optical microscopy, scanning electron microscopy and atomic force microscopy were performed. Fracture of the grains as well debris could be seen at the surface. X-ray diffraction was used to determine strain in the material via peak broadening showing an increase of strain in the ground samples. Furthermore cross-section investigation with scanning and transmission electron microscopy were performed. Binder phase depletion at the surface and subsurface as well as fracture and slip planes in the grains were observed. Via (S)TEM energy-dispersive X-ray spectroscopy and energy filtered transmission electron microscopy a tribofilm formation at the surface can be assumed.

Kurzfassung

Wendeschneidplatten aus gesintertem Hartmetall sind in der Zerspanung von Metallen ein unersetzbares Werkzeug. Hartmetall ist ein Sinterwerkstoff und besteht aus harten Carbid-Teilchen, die in einer metallischen Matrix, welche weich und zäh ist, gebunden sind. Zumeist wird Wolframcarbid und Cobalt als Binder verwendet. Die hohe Verschleißfestigkeit und der Härtegrad von Hartmetallen sind die idealen Eigenschaften in der metallzerspanenden Industrie. Dabei muss stets die Zuverlässigkeit und Genauigkeit der Wendeschneidplatten hoch gehalten werden. Erhöhte Genauigkeit wird durch Oberflächenbehandlung wie z.B. Schleifen erreicht. Diese geschliffenen Wendeschneidplatten können aber gegenüber ungeschliffenen eine verkürzte Standzeit aufweisen.

In dieser Arbeit wird ein Überblick über die bekannten Verschleißmechanismen von Wolframcarbid, Cobalt und WC-Co Hartmetall gegeben. Oberflächenuntersuchungen von geschliffenen und ungeschliffenen Hartmetallen wurden durchgeführt. Lichtmikroskopie, Rasterelektronenmikroskopie und Rasterkraftmikroskopie wurden verwendet. Riss- und Bruchbildung sowie kleinere Bruchstücke von Hartmetallkörnern ergaben sich an der Oberfläche. Röntgenbeugung zur Bestimmung von Eigenspannungen über die Linienverbreiterung ergaben eine Erhöhung von Eigenspannungen im geschliffenem Hartmetall gegenüber dem ungeschliffenen. Weiters wurden Querschnittsuntersuchungen mit Raster- und Transmissionselektronenmikroskopie durchgeführt. Neben Rissbildung und Versetzungen konnte eine Verarmung des Binderanteils an der Oberfläche sowie in oberflächennahen Bereichen festgestellt werden. (S)TEM energiedispersive Röntgenspektroskopie und energiegefilterte Transmissionselektronenmikroskopie lassen die Bildung eines „Tribofilmes“ an der Oberfläche vermuten.

Acknowledgement

At this point I want to acknowledge all people who made this thesis possible. Without their continued efforts and support, I would not have been able to bring my work to a successful completion.
I wish to thank my supervisor Prof. Werner Grogger for giving me the possibility to do this research and for his scientific guidance.
Deep gratitude also goes to my co-supervisor Evelin Fisslthaler for her tremendous support, enthusiastic encouragement and the useful critique during the whole work.
Furthermore I have to thank Stefan Mitsche for his support in operating the SEM and evaluating of the SEM and XRD measurements, Martina Dienstleder for her technical support and helpful discussions and Timothy Aschl for helping me to perform and evaluate the AFM measurements as well as for his technical assistance at the XRD.
I would also like to thank the laboratory staff especially Manuel Paller for his help in the laboratory, at the microscopes and for supplying me with graphics, Sebastian Rauch for his help during preparation and Julia Töglhofer for her moral support.
Not forgetting to thank all the people who were participating in the technical discussions about my thesis and their advices (Franz Schmidt, Nadejda Matsko, Daniel Knez, Florian Kolb and everyone I forgot)and of course the whole FELMI and ZFE team.
Last but not least I want to thank my family for their moral and financial support and of course all of my friends for being there.

Thank you!

Contents

1 Introduction and Motivation

Indexable inserts are widely used in industries for processing metals. Today these inserts are the workhorses in all areas of the manufacturing industries. An indexable insert is a symmetric cutting bit that has multiple cutting edges. Once a cutting edge is worn, it can be indexed to another edge or completely replaced easily (see figure 1.1). Tools

Figure 1.1: Different shapes of indexable inserts which can be screwed onto a tool holder [1]

for cutting should possess a high hardness and resistivity to obtain reliable, efficient and economical products. There are several different materials commonly used for these tools. The most common one consists of tungsten carbide (WC) particles which are embedded in cobalt (Co) as a binder phase. Tungsten carbide is a hard and brittle material but in combination with a soft binder it is an excellent tool for cutting, turning, drilling and milling of metals. These compounds are also called hard metals or cemented carbides.

The mechanical properties of such WC-Co alloys are dependent on various parameters. In hard metal the most important properties are the wear properties. They are related with the mechanical properties of the used materials such as hardness, ductility and fracture toughness. A lot of investigations were done to improve the wear properties of hard metals.

Most of the cemented carbide tools get ground to ensure close dimensional tolerances and good surface finish. In action it emerges that ground cemented carbides may possess a shorter life time than cemented carbides without this surface treatment.
The main objective of this study was to figure out why ground cemented carbides may have a shorter life time than unprocessed cutting tools that are fabricated from the same material.

2 Materials

The properties and manufacturing of the material used in this study is going to be explained. Furthermore an overview of defect formation processes, which were discovered by previous research, is given.

2.1 Cemented Carbide

Cemented carbides, also called carbid metal or widia (acronym for „WIe DIAmant“= like diamond), are wear resistant materials which are used for machining metals. They are combining hardness, strength and toughness at the same time. With a few exceptions their main component is tungsten carbide (WC). Titanium (Ti), tantalum (Ta) and niobium (Nb) as a carbide can also be present in the composition. These carbide grains get embedded in a ductile binder phase which is usually cobalt (Co). The binder phase can also be represented by an alloy of iron (Fe), chromium (Cr), nickel (Ni), molybdenum (Mo) and several other alloys.

In this study tungsten carbide (WC) with cobalt (Co) as a binder was used.

2.1.1 Tungsten Carbide (WC)

The Frenchman Henri Moissan produced W_2C in 1896 for the first time by using an electric furnace and around 1898 P. Williams produced tungsten monocarbide (WC) [2]. WC can be prepared by reaction of tungsten metal and carbon in a hydrogen atmosphere or in vacuum at 1400-2000℃ [3]:

$$W + C \rightharpoonup WC.$$

WC forms particles with varying sizes. The properties of tungsten carbide are determined by the purity and grain size. To receive fine grained powders ($< 1\mu m$) small amounts of vanadium (V), chromium (Cr) or tantalum (Ta) are added to the tungsten and carbon powders before carburization [4].

Tungsten monocarbide has a simple hexagonal crystal structure with two atoms per unit cell and with the lattice parameters $a = 0{,}2906\,\text{nm}$ and $c = 0{,}2837\,\text{nm}$ [5]. It melts at a temperature of $T = 2776$℃ [3] and has a density of $\rho = 15{,}63\,\text{g/cm}^3$ at 18℃ [6]. Stoichiometrically tungsten carbide has a carbon content of $6{,}13\,\text{wt}\%$. WC is about three times stiffer than steel, possesses a high hardness, but it is brittle. Due to the extreme hardness (1700-2400 Hv = Vickers number [7]) it is used in a compound as a cutting tool for machining .

Deformation mechanisms in WC

In tungsten carbide grains several slip planes are able to plastically deform the grain without the occurrence of brittle fracture. TEM investigations on bulk samples suggested that the slip planes are of the $(10\bar{1}0)$ type and the possible slip directions are $<0001>$, $<11\bar{2}0>$ and $<11\bar{2}3>$ [8–10]. Unit dislocations with the Burgers vectors $<0001>$, $\frac{1}{3}<11\bar{2}0>$ and $\frac{1}{3}<11\bar{2}3>$ have been observed and said to be glissile on a number of different planes [11]. In the recent past another study claimed that only the $(10\bar{1}0)<11\bar{2}3>$ system which produces slip equivalent to $(10\bar{1}0)<11\bar{2}0>$ and $(10\bar{1}0)<0001>$ is active in the WC [12]. There is only a four slip system available and this would limit the deformation of polycrystalline WC and can cause interfacial cracks. Nucleation of microcracks in WC grains can also be caused by glide of $\frac{1}{6}<11\bar{2}3>$ partials and is usually associated with slip in intense shear bands [13–15].

2.1.2 Cobalt (Co)

Cobalt has an atomic number of 27, was discovered by Georg Brandt in 1735 [16] and is found naturally only in chemically combined form (copper and nickel mineral ores). Due to reduction with carbon cobalt is produced as a byproduct of copper (Cu) and nickel (Ni):

$$Co_3O_4 + 2C \rightharpoonup 3Co + 2CO_2.$$

At temperatures below $T = 417$℃ cobalt possesses a hexagonal close-packed structure and in between $T = 417$℃ and its melting point $T = 1493$℃ it has a face-centered cubic structure [17]. Cobalt is a ductile metal and has a density of $\rho = 8{,}90\,\mathrm{g/cm^3}$ at $T = 20$℃ [18]. Mostly it is used as an alloying element to improve the high thermal stability and wear resistance of alloyed steels and as a binder phase in cemented carbides. In cemented carbides cobalt provides high densities because of its wetting or capillary action during sintering [19]. Another characteristic property that makes cobalt such an effective binder metal for cemented carbide is the relatively low melting temperature of cobalt-tungsten carbide and the solubility of tungsten carbide in cobalt [20].

Deformation mechanisms of Co as a binder in WC-Co alloys

The structure of the binder Co in WC-Co alloys is mainly fcc but this structure is unstable at room temperature. In the undeformed state the binder has numerous stacking faults. During deformation a martensitic transformation from fcc to hcp (hcp binder lamellae) takes place to lower the energy in the binder and is accompanied by twin formation [21–23]. In WC-Co alloys a complete transformation has never been observed. Since the fcc structure is unstable at room temperature the stacking fault energy becomes very low and therefore dislocations and stacking faults are the prominent feature in deformed samples [11]. In a previous study it was estimated that less than 10% of the binder transforms before fracture of the material takes place [24].

2.1.3 Production and Properties of Cemented Carbide WC-Co

As already mentioned only tungsten carbide (WC) with cobalt (Co) as a binder will be discussed.

It was in 1932 when Karl Schröter filed a patent for the production of a sintered WC infiltrated with Co [25]. Since then a huge market opened and today cemented carbides are the workhorses in all areas of the manufacturing industries.

General cemented carbides are sintered materials in which the brittle refractory carbides are bound by a soft ductile metal binder. The overall process to manufacture cemented carbides is called powder metallurgy (PM) and there are a lot of different production technologies. Mostly they involve the following steps:

1. Powder production,
2. Mixing of powders,
3. Forming/molding of the mixed powder,
4. Sintering to enhance integrity and strength
5. Secondary operations or rework.

How WC and Co are produced was already described in section 2.1.1 and 2.1.2. The mixing of powders is done in ball mills or attritors and has to be intense to ensure a good blending. Milling is done in the presence of a milling liquid (ethanol, acetone etc.) to prevent oxidation and minimize heating of the powder. Afterwards the milling liquid is removed by a spray-drying process. The forming of the powders is achieved by pressing to obtain a green compact with sufficient strength to withstand further handling operations. Before pressing an organic binder (paraffin wax) is added to the powder to improve the pressing properties and to impart strength to the pressed powder [4]. In the next step the organic binder is removed by heating the compact to about $T = 500$°C. Then sintering is performed, which can be done in vacuum or under atmospheric pressure with protective gas. The amount of the cobalt binder defines the final sintering temperature (mostly between $T = 1350 - 1500$°C [26]). During this process the cobalt melts and wets the tungsten carbide totally. The solids receive a shrinkage of 17-25% producing virtually pore-free, fully dense products [4]. Secondary operations include further pressing, grinding and coating. They are used to ensure close dimensional tolerances, good surface finish and an increase in life time.

The properties of the cemented carbide WC-Co are critically dependent on their final composition and structure [27]. Of course there are a lot of different properties of WC-Co so in this study just the most important are pointed out.

Hardness

The hardness of a material is the ability to withstand penetration by a surface contact, through a combination of plastic flow and brittle fracture. This property is the most important one when it comes to abrasion resistance. Both composition and microstructure

affect the hardness, therefore cobalt content and WC grain size have to be considered. For example at a given cobalt content the hardness increases with decreasing WC grain size(see figure 2.1(a)) [4]. Another value which affects the hardness is the contiguity. Contiguity is defined by the ratio of the grain boundary area shared by carbide grains to the total surface area of the grains [28].

Fracture Toughness

Fracture toughness describes the ability of a material featuring a crack to resist fracture. It is a measure of the energy required for mechanical failure. Since the binder phase is ductile the binder absorbs energy via plastic deformation. To increase fracture toughness a larger grain size is required (see figure 2.1(b)).

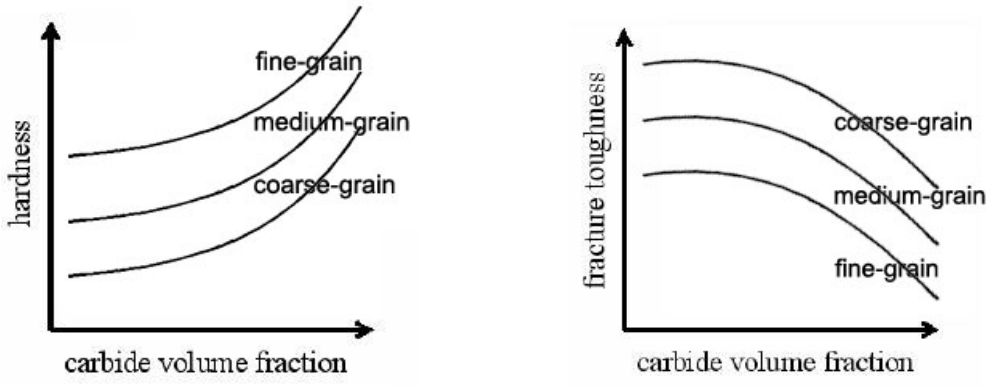

(a) (b)

Figure 2.1: Schematic diagrams of a) the hardness as a function of the carbide volume fraction and grain size and b) fracture toughness as a function of the carbide volume fraction and grain size (adopted from [29])

Transverse Rupture Strength

The transverse rupture strength (TRS) is determined by bending the cemented carbide until failure and is used to measure the fracture strength. The relationship between microstructure and TRS is not well established. A higher content of Co and smaller WC grains yield an increase in fracture strength [30, 31]. It was also shown that within a hardness range of $800 < Hv < 1500\,\mathrm{kg/mm^2}$, TRS appears to first increase and then decrease as the hardness increases [32].

Density and Porosity

The density of cemented carbides is very sensitive to composition and porosity in the specimen and is widely used as a quality control test [4]. Desirable are high densities to avoid pores which degrade the mechanical properties. Pores are caused by low carbon

content, inhomogeneous blending of the powders, trapped gases and impurities [33].

The carbon content is not only responsible for pores. If the phase diagram of the W-C-Co system is considered so called η-carbides with the composition $(W, Co)_6C$ can be formed. These phases are brittle and that is why the carbon content in WC-Co materials has to be treated carefully [34].

2.2 Friction and Abrasive Wear of WC-Co Hard Metals

WC-Co hard metals have been employed in a wide variety of fields since they were first developed. The hard metals are used in many wear resistant applications and that is why the processes and mechanisms of wear are a matter of scientific interest.

Up to the present there were a lot of studies of abrasive wear behaviour of WC based hard metals [35–49]. One of the first investigations used X-ray diffraction to examine plastic deformation in tungsten carbide [50]. Nowadays a lot of other techniques can be used to determine wear of cemented carbides. It has been shown that the abrasive wear rate of WC-Co hard metals mainly depends on the carbide/cobalt ratio and the size of the carbide grains [51]. The wear rate increases in proportion with the increase of the cobalt content [35–43] and the size of the carbide grains [41–49].

In previous studies several wear mechanisms under different conditions were discovered using various techniques. Their occurrence depend on a lot of parameters like the experimental technique, the intensity of the wear and which specimen was used. To receive an overview about the wear mechnisms some results of previous investigations are listed.

Residual Stress

In almost every material residual stress is present. There are various reasons from where they originate, including plastic deformations, temperature gradients during heat treatment or structural changes. Residual stress can be measured via several different techniques, which can be classified into non-destructive and destructive methods.

One of the first investigation of wear on blocks of sintered tungsten carbide was done with X-ray diffraction. Broadening of the peaks was observed and analysed by different methods. To obtain a distribution of the induced microstrain layers of the sample were electrolytically etched away and the observed peaks were analysed by the variance method [52,53]. This distribution for microstrain normal to the $(10\bar{1}1)$ planes can be seen in figure 2.2(a) [50]. This result in comparison with previous studies on milled powders shows that an increase of plastic deformation was taking place. The deformation extends to several microns below the surface. The plastic deformation causes work hardening, which results in the surface layers becomeing brittle and fracturing [50].

Another study which used X-ray diffracation to examine residual stress in WC-Co due to grinding obtained the same results [54]. The method was non-destructive without

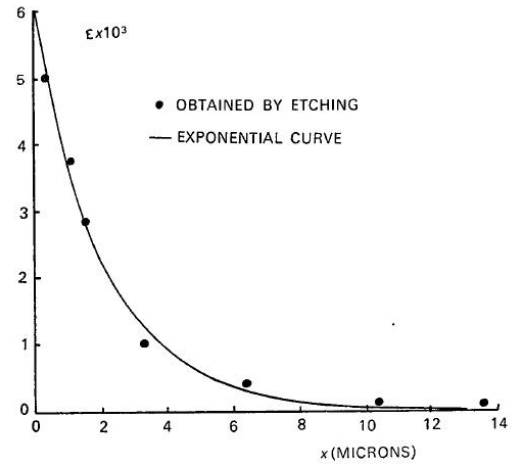

(a)

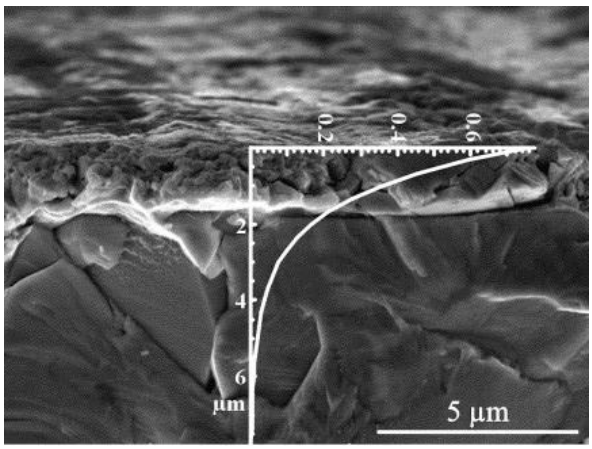

(b)

Figure 2.2: a) Distribution of microstrain ϵ below a worked surface (adopted from [50]); b) SEM image of the cross section at the ground surface including a graph of the intensity of the reflected X-rays as a function of depth $I(z)$ (adopted from [54])

etching and the $sin^2\psi$ method was used to calculate the stress. For the (201) reflection an increase of the stress could be measured and also for the average stress an increase was obtained [54]. It was also revealed that 50% of the measured radiation comes from the first 0,9 µm and that 95% appears from a depth of $< 3{,}9$ µm [54](see figure 2.2(b)).

The increase of the stress in WC-Co alloys can also be seen in TEM investigations. If WC-Co samples get prepared damage and defects can be induced. One sample preparation method is wedge polishing where mechanically electron transparent areas are achieved. Due to mechanical polishing the WC grains receive an increase of the defect density in comparsion to an ion polished sample (see figure 2.3(a) and 2.3(b)). TEM high resolution images (see figure 2.4) are showing that the crystalline structure of the grains is disturbed.

Similar results were observed at deformed cutting edges of WC-Co inserts. TEM observations showed a considerable deformation of the WC grains and some infiltrated grain boundaries were facetted along low energy planes (see figure 2.5(a) and 2.5(b)) [56]. Not only dislocations, stacking faults or twin formation could be found but also hcp binder lamellae. These hcp lamellae originate from the martensitic transformation of the binder (see also section 2.1.2). Examples of binder phase lamellae can be seen in figure 2.6. In figure 2.7 a binder lamella at higher magnification can be seen [56].

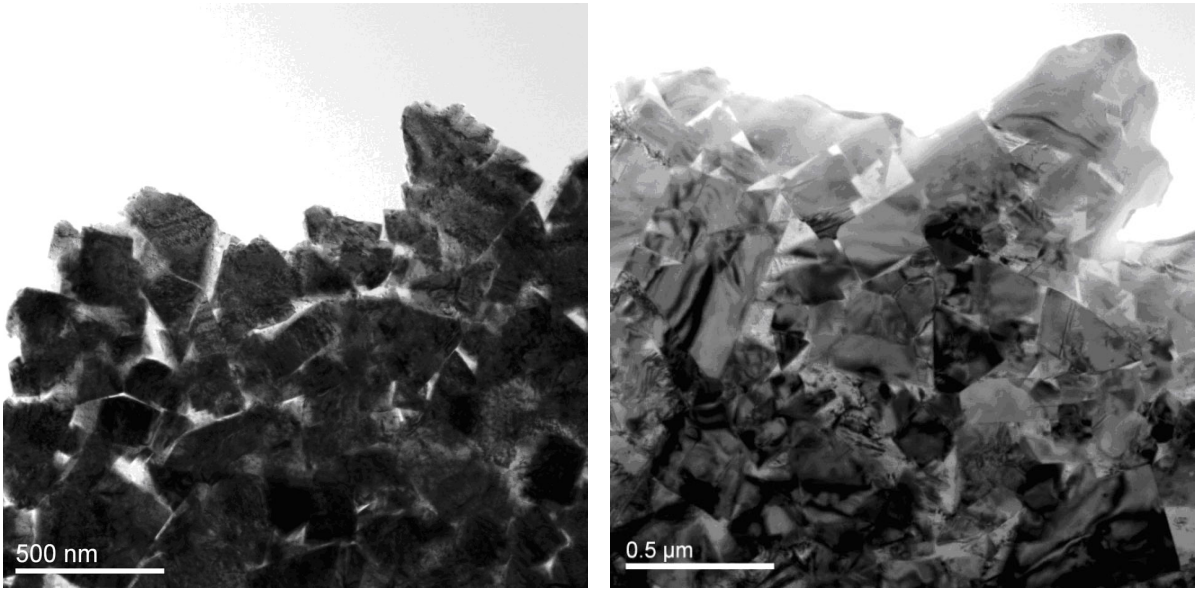

(a) (b)

Figure 2.3: TEM BF image of a WC-Co alloy a) wedge polished and b) ion thinned sample (adopted from [55])

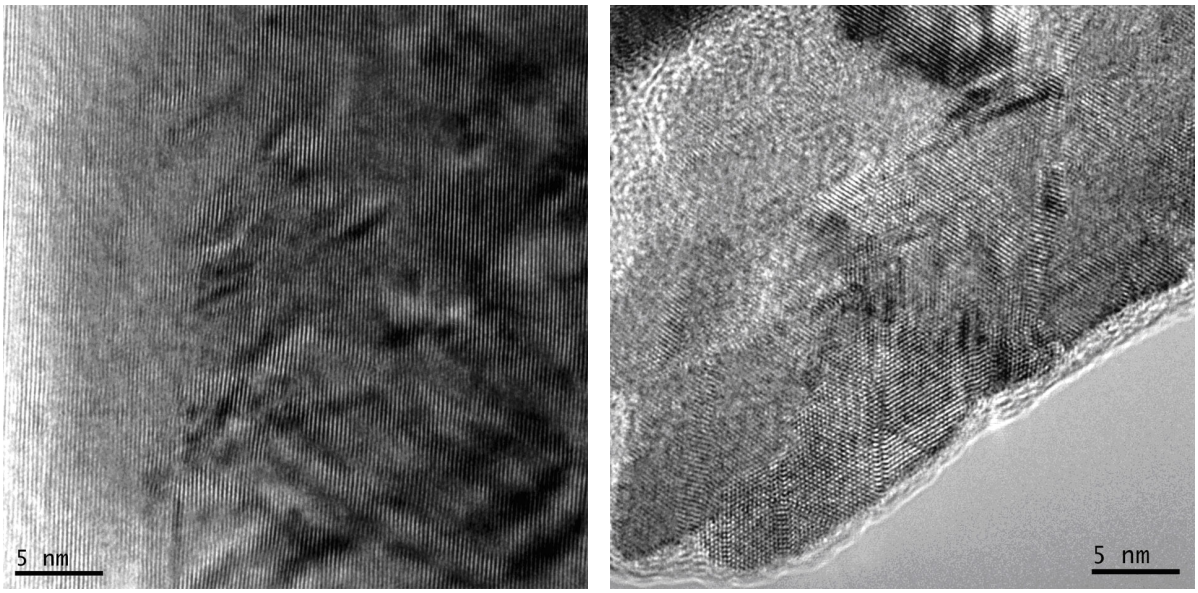

Figure 2.4: TEM high resolution BF images of a polished WC-Co alloy. Defects in the crystal structure can be seen (adopted from [55])

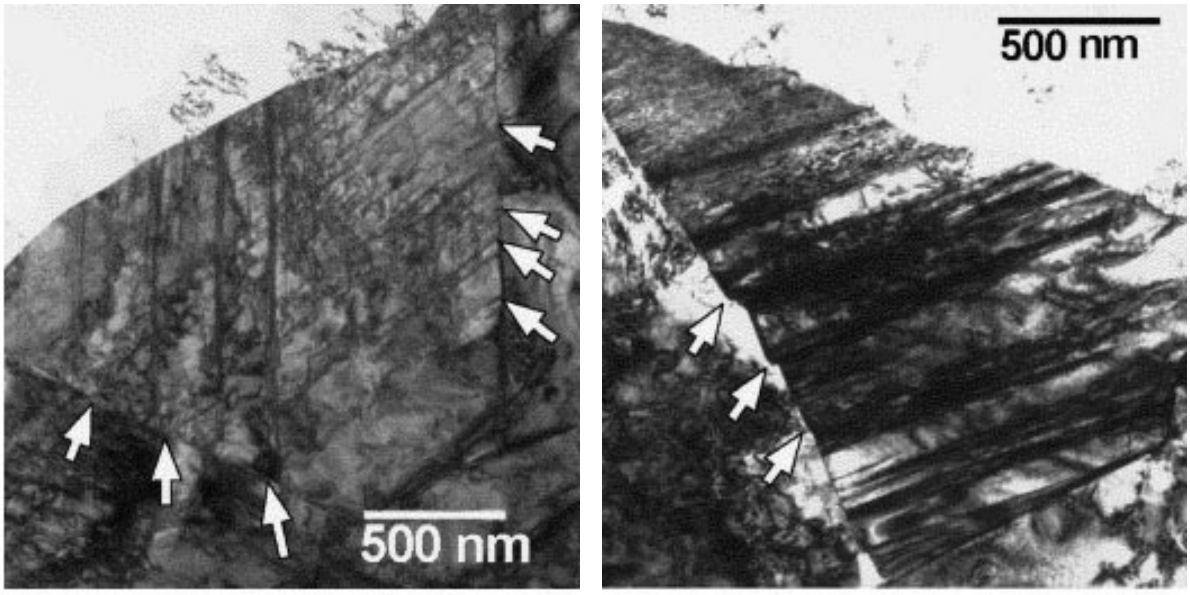

(a) (b)

Figure 2.5: TEM images of a plastically deformed WC grain; a) grain seems to be deformed along two plane directions, b) slip lines and steps have formed at grain surface (arrows) (adopted from [56])

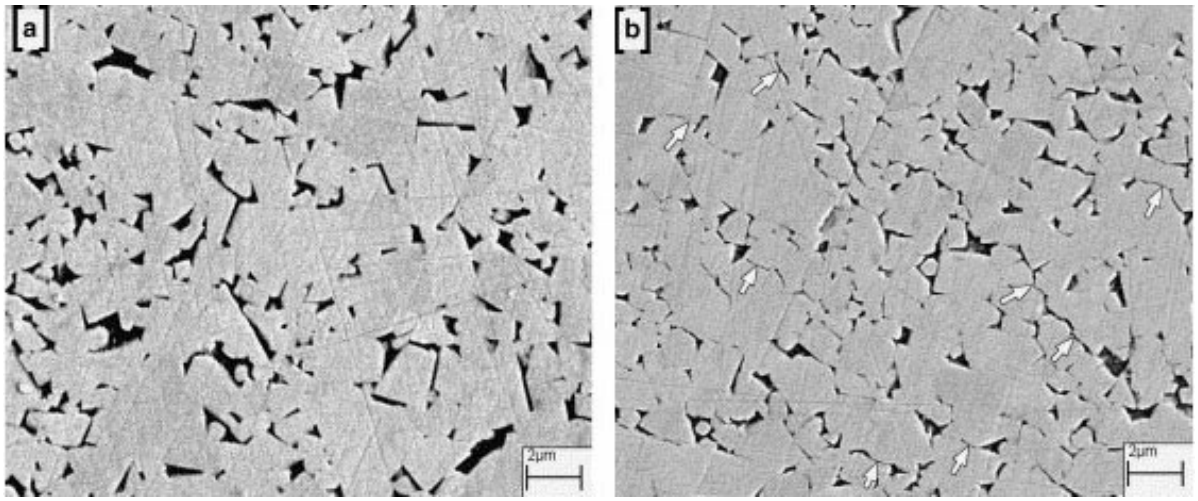

Figure 2.6: SEM images of an **[a]** undeformed and **[b]** deformed WC-Co, examples of binder phase lamellae are marked with arrows (adopted from [56])

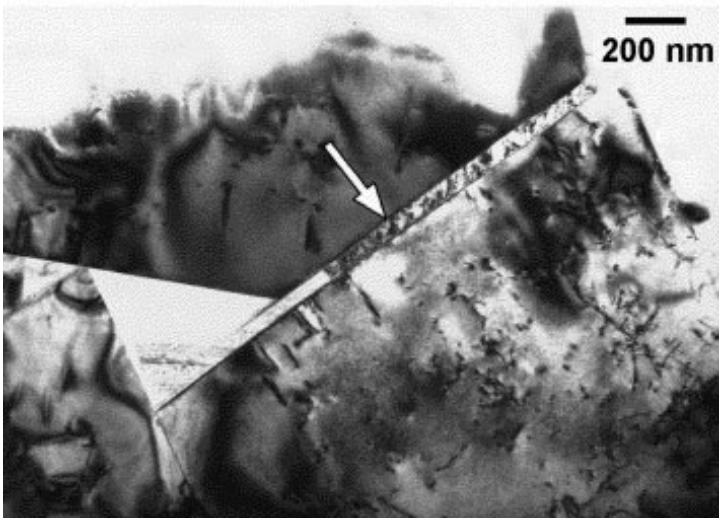

Figure 2.7: TEM image of a binder lamellae marked with an arrow (adopted from [56])

The new hcp structure possesses only one slip plane and further deformation becomes increasingly difficult.

Microcracks and Fracture

If the deformation progress proceeds the binder can not any longer prevent cracks because of the constrained movement of the slip plane in the hcp structure. This causes a crack formation in the binder and a simultaneous break up of the WC grains. There are actually four different types of fracture paths which can be distinguished in WC-Co alloys [57]:

1. transgranular fracture through the carbide grains,
2. along carbide grain boundaries,
3. transgranular fracture through the binder phase (Co) and
4. along binder/carbide boundaries.

A general agreement is that most of the fracture energy is dissipated into transgranular fracture through the binder phase. Usually the carbide fracture precedes binder fracture and therefore determines the direction and type of path the crack takes [57]. In previous work of wear under dry abrasive conditions microcracks can be seen at the worn surface [58](see figure 2.8(a)). Another study used a diamond abrasive wheel with a water-oil emulsion as a coolant. Slip lines and cracks in the WC grains at the surface could be observed (see figure 2.8(b)).

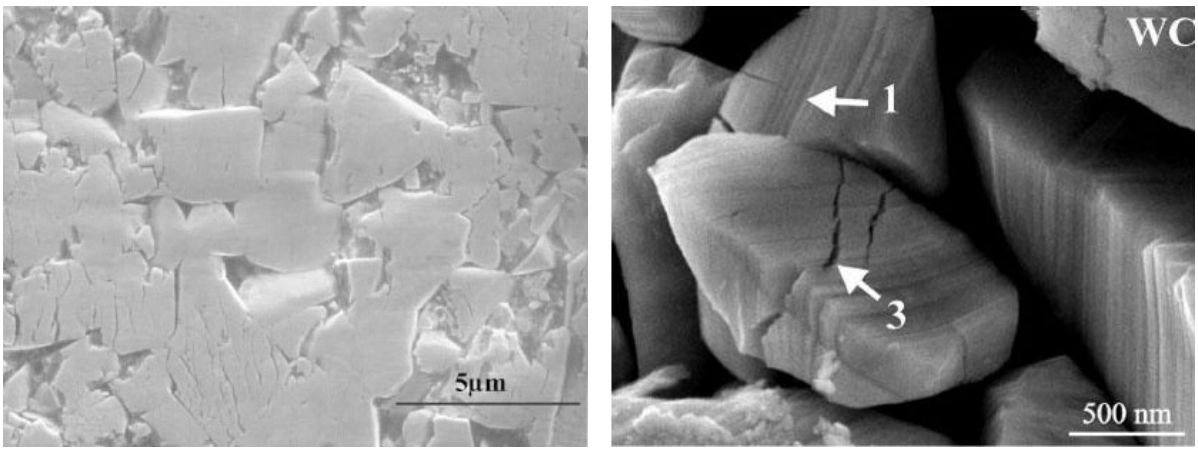

(a) (b)

Figure 2.8: SEM image of a worn surface of a WC-Co hard metal a) with 6,09% Co content (adopted from [58]) and b) with 10% Co content, 1) slip lines and 3) cracks found in a WC grain (adopted from [54])

Binder Phase Extrusion, Carbide Grain Fall-out and Tribofilm Formation

During wear studies it was found out that a binder depletion takes place [46, 59, 60]. This extrusion can be explained by a network of microcracks through which the binder is pushed out. A binderless subsurface is left and fall-out of carbide grains appears. In several studies a layer covering the surface was observed [54, 61–63]. This layer is called tribofilm and consists of small carbide grains and some binder phase. In figure 2.9(a) a ground WC-Co surface can be seen with areas of debris which is covering the surface. Cross section analysis can be seen in figure 2.9(b). The size of the carbide grains in such

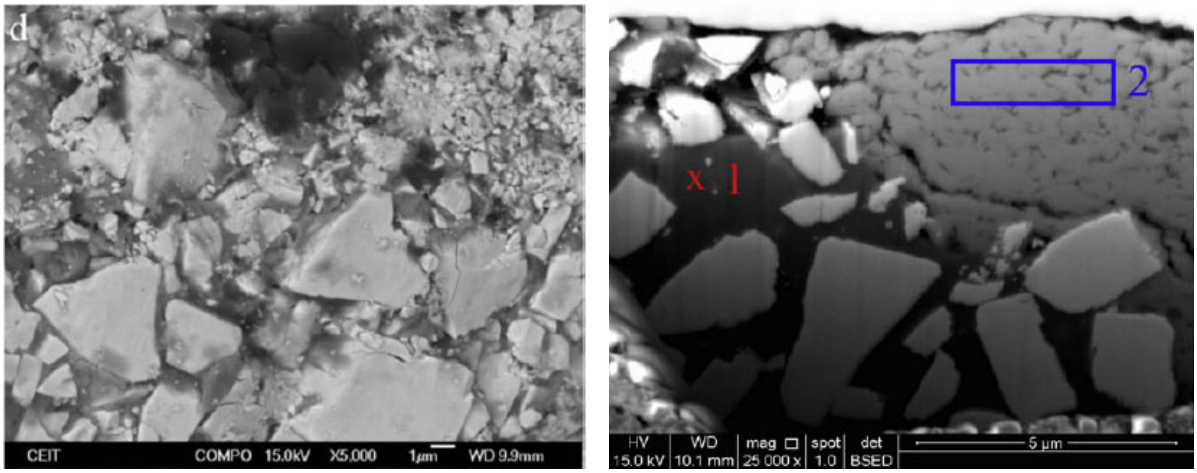

(a) (b)

Figure 2.9: SEM image of a worn WC-Co hard metal: a) surface (15% Co content); b) cross section with tribofilm (25% Co content) (adopted from [63])

a tribofilm is remarkably small in comparsion to the usual size and the binder content is lower than in the bulk region. Also it showed up that there is a sharp transition between the smooth outer surface and the unevenly worn WC grains beneath the tribofilm (see figure 2.9(b) and 2.2(b)).

Further investigation via TEM revealed that the carbide grains in a tribofilm receive a round structure (see figure 2.10(a) and 2.10(b)) [62]. These small grains originate from fracture or fall-out of WC grains and get re-embedded onto the surface. With proceeding wear they get rounded. Same results were obtained with AFM measurements. Tribofilms

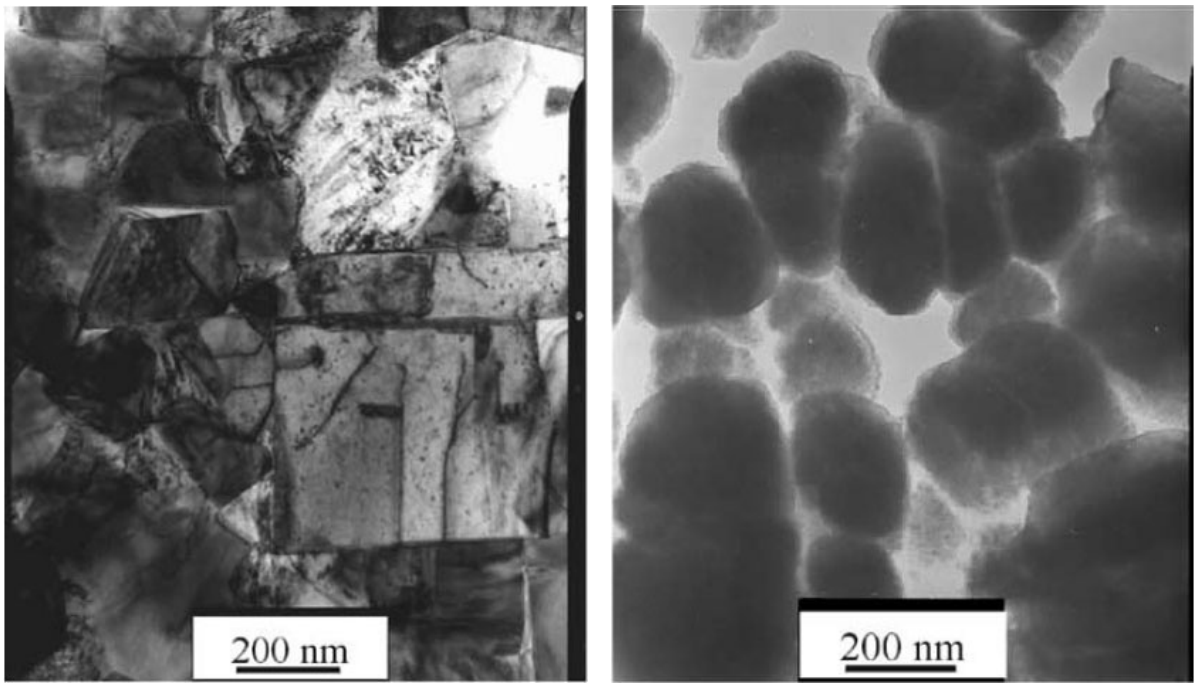

(a) (b)

Figure 2.10: TEM images of worn hard metal a) bulk material b) top view on tribofilm (adopted from [62])

can act like a lubricant and therefore they can reduce the wear rate.

2.3 Grinding of Hard Metals

As already mentioned in the section about the production of cemented carbides (see section 2.1.3) sintered WC-Co hard metals might receive different types of rework to ensure close dimensional tolerances, good surface finish and an increase in life time. However, here just the grinding process is going to be pointed out because the effect of grinding onto the hard metal is the major task of this study.

Mainly grinding is performed to ensure close dimensional tolerances and surface finishing. During sintering the hard metal receives shrinkage and this causes deviations of

the desired shape of about ±3% [64]. Therefore grinding is used to satisfy the dimensional tolerances. Especially the cutting edge has to be accurately shaped to obtain the required tolerances and surface quality. Also during operation worn cutting edges can be ground to reuse them.

Grinding is done with CNC grinding machines equipped with diamond disks. As coolant water, oil or synthetic based fluids can be used. All of them possess different properties and have a different application. It should be pointed out that some water based coolants can leach the cobalt out of the cemented carbide.

Due to improving the forming and sintering process of cemented carbides grinding is not so often necessary than in the past. However, during operation it can be observed that ground cemented carbides may possess a shorter life time than unprocessed cemented carbides.

3 Fundamentals and Methodology

First of all a short description about different techniques which can be used to determine defects in the specimen is given. More precisely the method to examine crystal defects with a transmission electron microscope and with X-ray diffraction are specified.
Also specimen preparation techniques are going to be explained shortly.

3.1 Methods of Investigation

3.1.1 Transmission Electron Microscopy

In transmission electron microscopy (TEM) electrons get emitted by an electron source (field emission gun or thermionic gun) and transmitted through a very thin specimen (around $< 50 - 100\,\text{nm}$) [65]. Within the specimen the electrons interact with the mate-

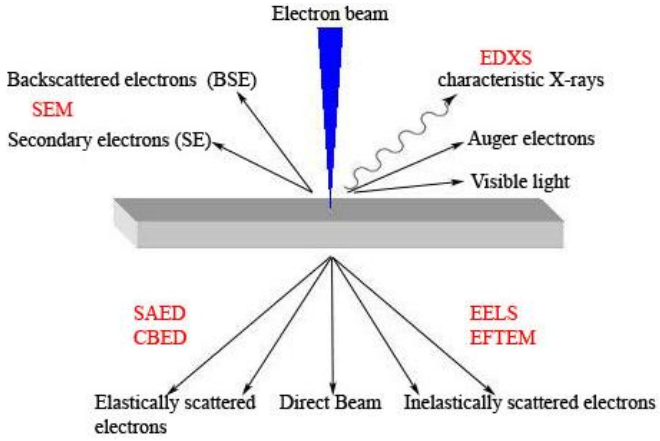

Figure 3.1: Occuring interactions of the electrons with the specimen

rial (scattering, diffraction, transmission and backscattering) and can give information about the structure and the chemical composition (see figure 3.1). This 3D-information gets projected on a viewing screen (fluorescent screen, CCD-camera or photographic film). So a TEM presents a 2D image of a 3D object and all of this information gets averaged through the thickness of the specimen. The guidance and focusing of the electrons is done by various electromagnetic lenses and the whole microscope operates in vacuum to increase the mean free path of the electrons outside the specimen.

There are two different imaging modes in TEM, bright field (BF) and dark field (DF). For obtaining a BF image a small aperture gets inserted to intercept the diffracted

beam which only allows the transmitted beam to form an image. Alternatively, the aperture can be displaced from the optic axis and only the diffracted beam forms the image, which is called DF imaging. If an image is formed without the aperture the contrast will be poor. But there is also the possibility to do spectrometry, like energy-dispersive X-ray spectroscopy (EDXS), electron energy loss spectroscopy (EELS) and energy filtered transmission electron microscopy (EFTEM). In a different adjustment of the lenses a diffraction pattern of the specimen can be obtained. This is called diffraction pattern (DP) but usually a selected area electron diffraction (SAED) aperture is inserted. Imaging combined with spectrometry is called analytical TEM (AEM).

It is also possible to use a convergent electron beam and scan over a defined area of the specimen (scanning transmission electron microscopy, STEM). This offers the option to obtain BF-, annular dark field- (ADF) and high-angle annular dark field (HAADF) images. It is also possible to obtain point analyses of the specimen with EELS and EDX.

Selected Area Electron Diffraction

When a beam of electrons passes through a crystalline specimen diffraction takes place. It creates a diffraction pattern (DP) on the viewing screen by the elastically scattered electrons. With the DP basic crystallographic information can be provided such as the orientation of the specimen, orientation relationships between crystals and the distance between the atomic planes. Using a SAD aperture determines the analyzed specimen area.

X-Ray Spectroscopy

The accelerated electrons in the microscope can eject an inner shell electron from an atom of the specimen. When this shell gets filled by outer, higher-energy shell electrons characteristic X-ray emission may occurs. These characteristic X-rays can be measured by an energy-dispersive spectrometer and the elemental composition of the specimen can be determined. EDXS works best for heavier elements. The beam electron, which ejected the shell electron, loses energy but continues through the specimen (inelastic scattering).

Electron Energy Loss Spectroscopy

For EELS the inelastically scattered electrons get bent by a magnetic prism inside an EEL spectrometer. This prism seperates the electrons according to their energy loss. With an energy loss caused by an inner shell ionization one can determine the atomic composition and the chemical bonding. EELS tends to work best for light elements and is therefore a complement to EDXS.

Energy Filtered Transmission Electron Microscopy

In EFTEM the electrons get also seperated according to their energy but an additional energy selecting slit gets inserted. With aligning the energy selecting slit to specific

energy values it is possible to just let pass electrons with a certain loss of energy which is specific for an element. This means one can determine the elemental distribution of the specimen as long as it is very thin. A thickness map can also be achieved by computing an image formed by the „zero loss“ electrons and an image without an energy selecting slit.

For obtaining an elemental distribution map the three-window or the jump-ratio method can be used. In the three-window method two pre-edge images and a post-edge image are acquired. With the two pre-edge images the background can be calculated and gets subtracted from the post-edge image in order to obtain an elemental distribution map. The jump-ratio method uses the ratio between the post-edge and the pre-edge image, which significantly reduces diffraction contrast.

High-Angle Annular Dark Field

For obtaining high-angle annular dark field (HAADF) images the TEM has to be operated in STEM mode. The detector has the shape of an annulus and detects high angle, incoherently scattered electrons. Z-contrast is achieved because this technique is highly sensitive to variations in the atomic number of atoms.

3.1.2 Crystal Defects and Image Contrast in TEM

There are three main different contrast formation mechanisms in TEM:

- mass thickness (incoherent elastic scattering),
- diffraction (coherent elastic scattering) and
- phase contrast.

Diffraction contrast is a dominant mechanism for imaging dislocations and defects in crystalline specimen, but also phase contrast and a change in effective thickness can occur [66]. Especially if there is a high defect density the strain fields overlap and a proper analysis is quite difficult. Characterization should always start from the diffraction pattern followed by bright and dark field imaging. To receive the best contrast the specimen should be tilted in such a way that only one diffracted beam is strong and the direct beam is the other strong spot (two-beam criterion) [67]. Therefore a double tilt holder is essential.

The most important microstructure features and crystal defects include [66]:

1. Changes in orientation with or without change in structure composition (grains, twins, structure of boundaries)
2. Lattice defects (point-, line-, planar- and volume defects)
3. Multiple-phase systems (changes in composition or structure or both).

Most of these defects can be observed by diffraction contrast without operating the microscope at the highest resolution, which is a huge advantage. A diffracted beam is formed if the Bragg equation is satisfied

$$n\lambda = 2dsin(\theta) \tag{3.1}$$

where λ is the wavelength of the incident radiation, d the spacing of the atomic planes, θ the angle between the incident radiation and the atomic planes and n is an integer. To receive the image contrast a calculation of the intensity of the direct and diffracted beam is necessary. But these calculations are difficult to handle because re-diffraction of the diffracted beam can occur. As a solution a two beam dynamical theory of image contrast has been developed [68], but mostly the kinematical theory [69], which is not dealing with re-diffraction, fits well with the experimental results.

Using the kinematical theory the intensity of the diffracted beam oscillates as a function of the thickness. A crystal imperfection is implied with a displacement $\mathbf{R}$ of the unit cell from its lattice position. The resulting difference is just a term $\mathbf{g} \cdot \mathbf{R}$, where $\mathbf{g}$ is the position of the diffracted beam. This is the $\mathbf{g} \cdot \mathbf{R}$ criterion and the visibility of most defects can be understood by this term. If there is for example a dislocation and the displacement $\mathbf{R}$ is perpendicular to $\mathbf{g}$ then $\mathbf{g} \cdot \mathbf{R} = 0$ so the dislocation is invisible.

Of course in real specimen the determination is not so easy but there is a lot of literature which offers classifications of different defects and some combinations of these [66, 67].

3.1.3 X-Ray Diffraction

X-ray diffraction is a fast and non-destructive method to measure the chemical composition and crystallographic structure of a material. When a monochromatic X-ray beam is projected on a crystalline specimen diffraction takes place if Bragg's law is satisfied (equation 3.1). By tilting the specimen the angle can be varied so that different Bragg conditions are satisfied. Detecting and plotting these occuring peaks via the angular position allows determination of the material because the peaks are characteristic for each material. The limiting factors are the X-ray source, which should be monochromatic, and the wavelength of the X-rays.

XRD can be used to determine the strain density and the crystallite size of the scanned specimen due observed peak broadening. There are mainly three factors which cause peak broadening:

1. Instrumental broadening,
2. Crystallite size broadening and
3. Strain broadening.

Instrumental broadening has its origin in non ideal optics, wavelength dispersion, sample transparency, axial divergence, flat sample effects and in the detector resolution. The crystallite size broadening increases with decreasing crystallite size. Strain in materials

can be uniformly and non-uniformly distributed. For uniformly distributed strain the unit cell expands in an isotropical way and this causes peak shifting but no broadening. If the strain is non-uniformly distributed it causes broadening due to defects in the material.

Scherrer showed at first how to calculate the mean crystalline size D using the line broadening at half the maximum intensity (FWHM) [70]. Later on Stokes and Wilson also used a relation with the FWHM for determining the lattice strains η [71]. Williamson and Hall then used these two equations to develop an equation which can seperate the size broadening and strain broadening effect [72]:

$$B \cdot cos(\theta) = \frac{k\lambda}{D} + \eta \cdot sin(\theta) \tag{3.2}$$

where B is the peakwidth (FWHM), θ is the angle between the incident and the scattered ray and k is the Scherrer constant and has a value of 1 in case of a $\theta/2\theta$ scale. If then $B \cdot cos(\theta)$ is plotted against to $sin(\theta)$ it will yield a straight line with a y-intercept equal to wavelength divided by crystallite size and a slope equal to the value of the microstrain.

Later on Wilson [73] modified this equation by using the integral breadth β of a peak instead of the FWHM B

$$\beta = \frac{A}{I} \tag{3.3}$$

where A is the area beneath the peak and I is the height of the peak.

3.1.4 Scanning Electron Microscopy

A scanning electron microscope (SEM) is used for compositional and topographical imaging and to determine the chemical composition of the specimen. Electrons get emitted from a cathode, are focused by electromagnetic lenses and are scanned over the surface of the specimen. These electrons then cause signals, like back-scatterd electrons (BSE), secondary electrons (SE), characteristic X-rays, light and specimen current, resulting from interactions between the electron beam and atoms at or close to the surface (see figure 3.1). SE and BSE are commonly used for imaging specimens.

SE are low energy electrons ($< 50\,\mathrm{eV}$) and originate from a thin surface layer. They get ejected by the incident electron beam through inelastic sacttering and are detected by an Everhart-Thornley detector. So they provide information about the topography of the specimen.

BSE are high energy electrons and these electrons originate from the beam which got backscattered by the sample and they penetrate deeper into the specimen. BSE can provide information about the distribution of elements (atomic number contrast). Material specific information can be obtained because heavier elements yield more BSE than lighter ones. The detection is done by solid-state devices, which have a ring-like shape and are located above the specimen.

3.2 Specimen Preparation

The first step to obtain good images and results with SEM and TEM requires a proper specimen preparation. There is a large variety of common preparation techniques so only the applied techniques will be listed (further information in [74]).

Which preparation is going to be used depends on the applied material and on the desired areas of investigation. In case of the ground cemented carbide a study of the surface and the cross-section is worthwhile, but not all methods of investigation require preparation.

Plan View Preparation

The plan view preparation is a technique which is used for TEM studies and it allows a investigation of the specimen surface.

First a disc of 3 mm diameter has to be cut out of the material. This can be done by an ultrasonic disc cutter. Afterwards the disc gets mechanically ground from the bulk side to a thickness of about 120 µm and then it will be dimpled to about 16 µm at the thinnest area. Finally electron transparent areas are formed by ion milling from the bulk side with two argon guns under a low angle.

Sandwich Cross-Section Preparation

This technique is much more time consuming than the plan view preparation and has a lot of different steps. As the name already mentions the observation direction will be transversal (cross section) to the surface.

A TEM sandwich compound exists of a ceramic, aluminium(III) oxide Al_2O_3, ring and a ceramic cylinder with a slit. This serves as a mechanical stabilisation of the sandwich. Inside the slit two plates with the surface of interest are glued together. From this tube 250 µm thin discs are cut off, which are then prepared as described above. As a next step a dimpler thins the disc from one side to a thickness of 16 µm. The final thinning is done by ion milling with two argon guns under a low angle.

Ion Beam Cross-Section Polishing System

This is a device to perform specimen cross-section preparation for SEM [75]. Argon atoms are used for polishing the specimens. First the specimen has to be placed with the surface of interest onto a blade by a conductive silver paste with a slight overhang around 70 µm. It has to be ensured that the conductive silver paste is not covering the edge of the blade to prevent contamination of the specimen. This blade is placed into the ion beam polishing system. The angle of the incident ion beam and the accelerating voltage can be chosen. Lower accelerating voltages ensure as gentle as possible polishing of the specimen, but also increase the polishing time. In figure 3.2(a) a schematical drawing of the polishing process can be seen. From the source the argon beam diverges and hits the specimen and the blade. Material of the specimen as well of the blade gets sputtered off. In figure 3.2(b) a shematical drawing of the polished area can be seen.

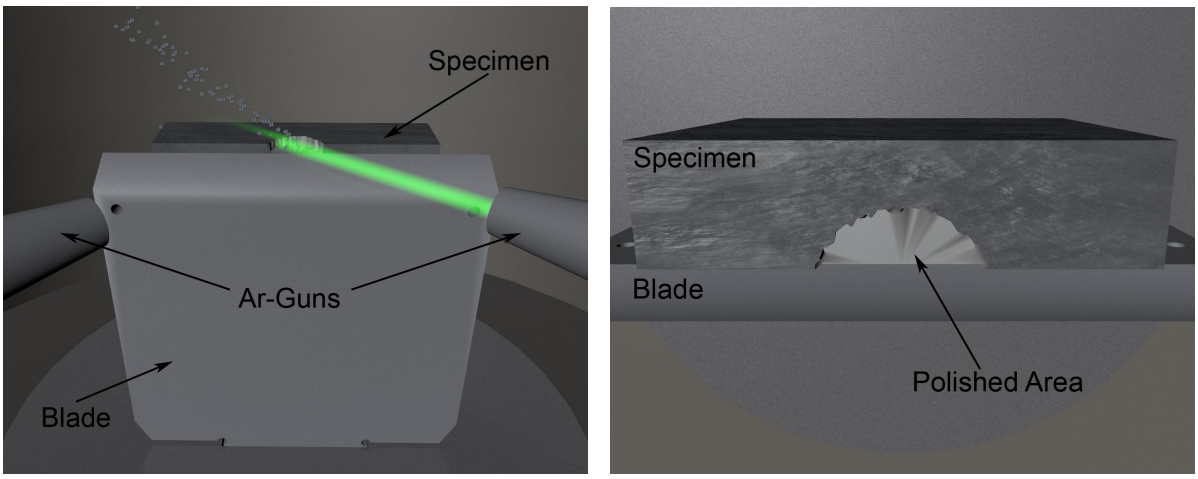

(a) (b)

Figure 3.2: a) Schematically drawing of the polishing process; b) top view of the polished area

Due to a small gap in between the blade and the specimen, sputtered off material can be trapped there and cause re-deposition. The surface of the specimen can be coated prior to the polishing process to distinguish between the real surface and the re-deposited material. It is also possible to place the specimen with the bulk surface onto the blade and polish through the whole specimen. This avoids re-deposition on the specimen surface of interest without coating the specimen, but it prolongs the process.

The advantage of this preparation technique is that a huge cross-section area (several $100 - 1000\,\mu m^2$) can be exposed within a short time. Repolishing after an observation is easily possible.

Focused Ion Beam Lamella

Focused ion beam (FIB) specimen preparation is an interesting technique for TEM specimen preparation because it is possible to select the area of examination precisely.

To obtain a TEM lamella for cross section investigation the specimen is placed into the FIB chamber. The size of the specimen can be quite small because the measures of the lamella are in µm the range. Platinum is placed over the region of interest to cover and protect the surface of the specimen. In a next step the lamella is produced by FIB milling and is lifted out with a fine needle. Afterwards the FIB lamella is fixed on a TEM grid and is now fit for use [76].

4 Experimental

4.1 Materials

The materials, which were used for investigation, were manufactured by „TRIBO Hartmetall“. All of these conventional cemented carbides are used for indexable inserts and possess a composition as shown in table 4.1. Four different samples were investigated

Table 4.1: Composition and properties of the investigated materials

Material notation	Grain size µm	WC content %	Co content %	Ground
WC1G	0,6	90	10	X
WC1	0,6	90	10	
WC2G	2,5	89	11	X
WC2	2,5	89	11	

according to their grain size. WC1 and WC1G possess fine grained tungsten carbide of $d = 0{,}6\,\mu m$. WC2 and WC2G possess a coarser tungsten carbide grain size of $d = 2{,}5\,\mu m$. For each material there is a sample which received no surface treatment and are so called sinter raw (WC1 and WC2). The other samples were ground with a diamond disk and metallic emulsion as a coolant (WC1G and WC2G). All of these cemented carbides were delivered as slices with a dimension of about 10 mm x 30 mm x 250 µm. These slices were cut off by electrical discharge machining from the inserts.

4.2 Surface Analysis

In all surface studies a preparation was not required and so the specimens were not affected by a preparation step. SEM and AFM were the two methods which were used for surface analysis. XRD was carried out as well and also here no preparation is required.

To obtain an overview of all sepecimen surfaces first an investigation with an optical microscope was performed. In figure 4.1 all surface images of the specimen can be seen. The fine grained cemented carbides WC1 and WC1G show no differences at this magnification. Both surfaces possess an uneven topography and WC1G shows no evidence that a grinding process has happened. For the coarser cemented carbides WC2 and WC2G a clear distinction is possible. The unprocessed cemented carbide WC2 shows a stained

surface with darker and brighter spots. Clearly grinding grooves due to grinding can be

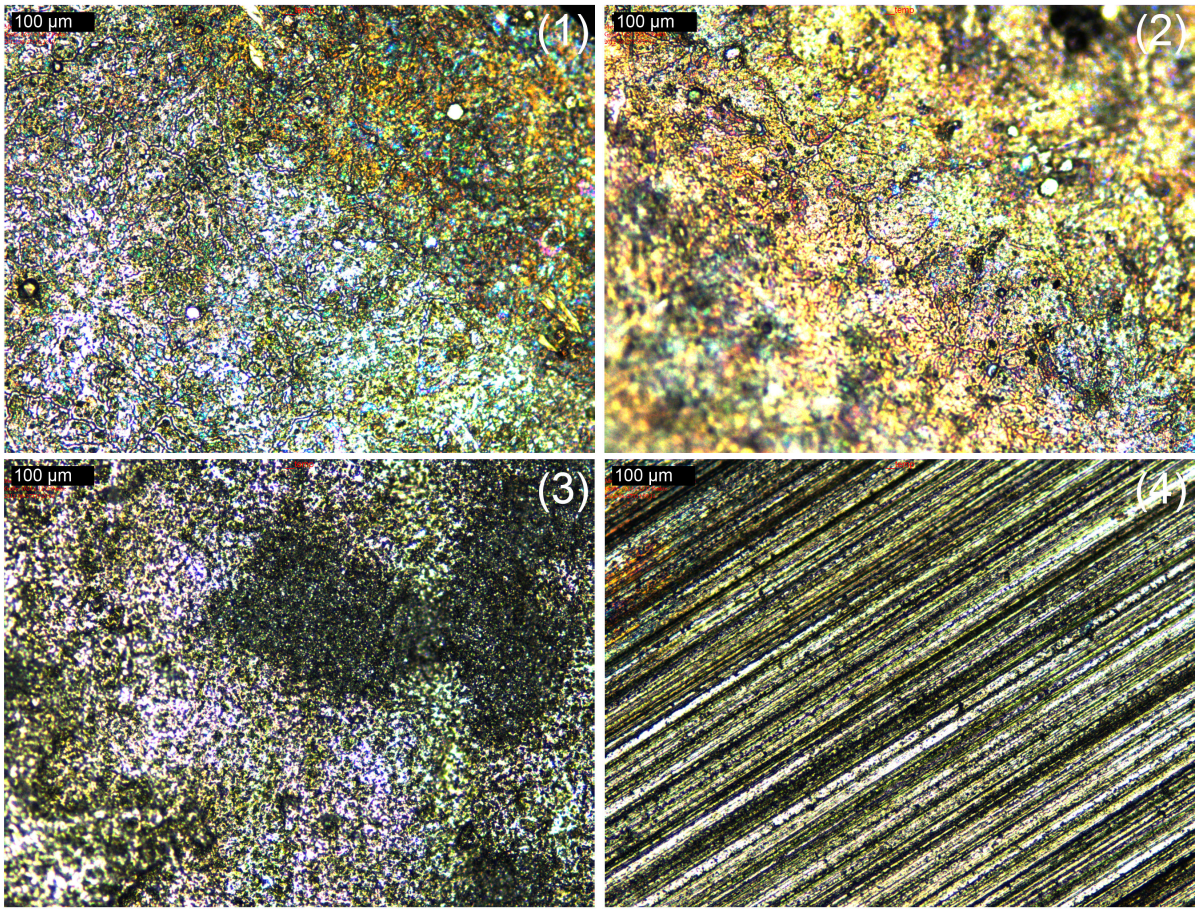

Figure 4.1: Optical microscope images at 20x magnification for (1) WC1 (2) WC1G (2) WC2 (4) WC2G

seen at the surface of WC2G and the stained surface is not anymore present.

4.2.1 SEM

SEM images were acquired at two different magnifications (1000x and 4000x).

The SEM measurements were performed on a FEI ESEM Quanta 600 FEG and the obtained data were analysed with the xT microscope control software.

Material: WC1 and WC1G

First the cemented carbide specimen with the finer grain size WC1 and WC1G were examined (see figure 4.2(a) and 4.2(b)). A solid state detector (SSD) is used to show elemental contrast. At this magnification a difference between the raw and ground specimen can not be seen. Both of them show a surface which is mostly covered by the binder phase (Co) and some spots where the tungsten carbide (WC) grains can be seen.

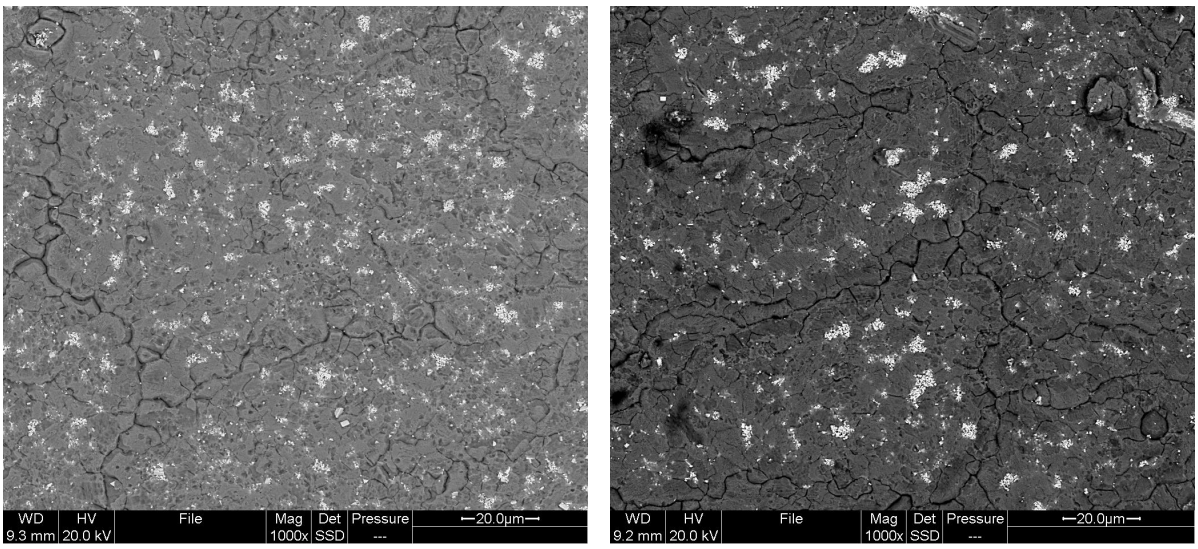

(a) (b)

Figure 4.2: SEM images (BSE) with elemental contrast of the cemented carbides a) WC1 and b) WC1G

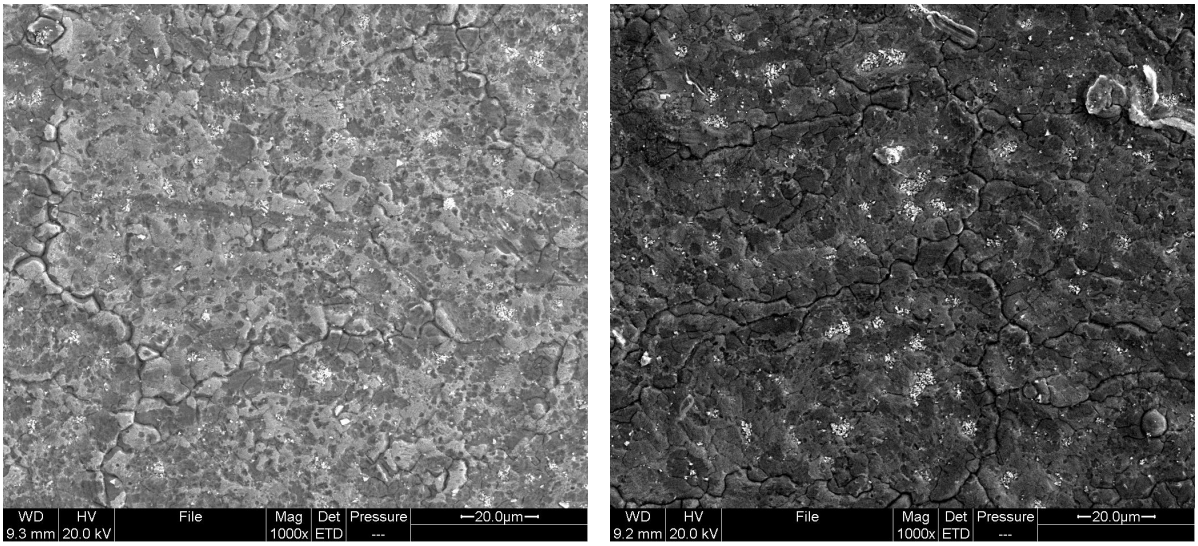

(a) (b)

Figure 4.3: SEM images (SE) with topographical contrast of the cemented carbides a) WC1 and b) WC1G

Also flaws are characterising the surface of both of the cemented carbides. These flaws can originate from the manufacturing process. Before sintering the mixed up powders are uniaxially pressed into shape. Because the pressing process is uniaxial a fraction of the applied pressure is transmitted to the walls of the form. These frictional forces between the powder and the form lead to pressure gradients within the insert and after

releasing the pressure this can cause flaws at the surface. Also in the images 4.3(a) and 4.3(b), which are showing topographical contrast, no significant difference can be observed.

At higher magnification basically similar results were obtained (see figure 4.4(a) and 4.4(b)). So no difference between these specimen can be seen, neither in different contrast

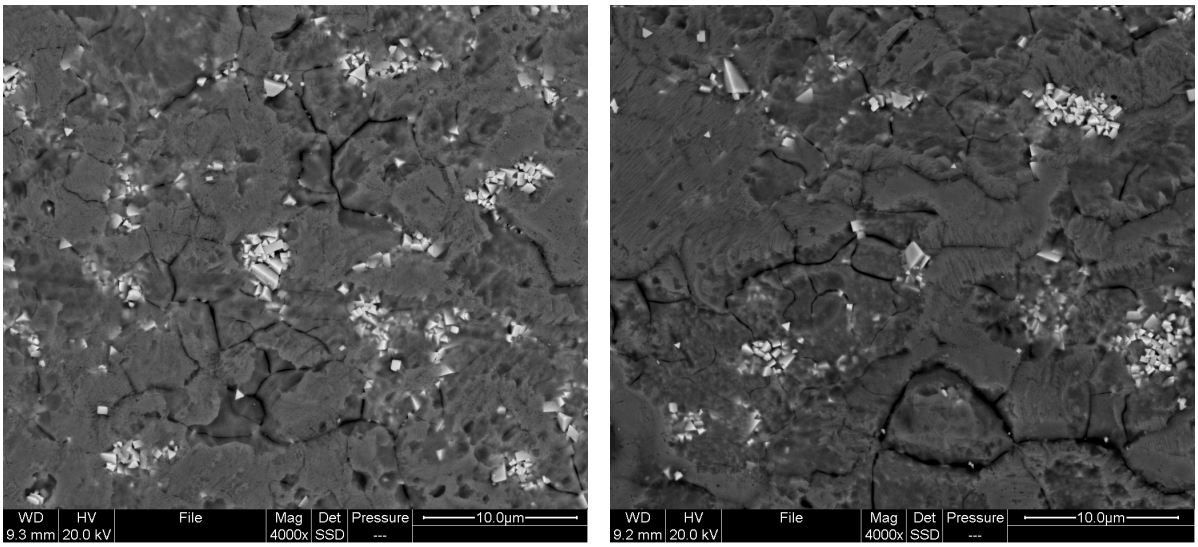

(a) (b)

Figure 4.4: SEM images (BSE) with elemental contrast of the cemented carbides a) WC1 and b) WC1G

nor at different magnification.

Material: WC2 and WC2G

For the coarser cemented carbide WC2 and WC2G images with the same magnification were acquired (see figure 4.5(a) and 4.5(b)). In figure 4.5(a) of the sinter raw cemented carbide WC2 are also two characterising features. There are areas on the surface which are covered by the binder phase (Co) and areas where the tungsten carbide can be seen. Large areas (several μm^2) with binder phase on top are called cobalt lakes (see figure 4.5(a)). This can happen during routine vacuum sintering and is caused by the incomplete distribution of cobalt in the sintering process. In this condition the binder is squeezed into macrovoids and forms this enrichments of cobalt.

The ground cemented carbide WC2G does not has these specific areas (see figure 4.5(b)). All over the surface the contrast is quite homogenous and the cobalt lakes are not visible. To show the characteristic features of WC2G a different detector is used, which shows topographical contrast (see figure 4.6(a) and 4.6(b)). With this detector the grinding grooves from grinding the cemented carbide in comparison to the sinter raw cemented carbide can be seen (arrows in figure 4.6(b)).

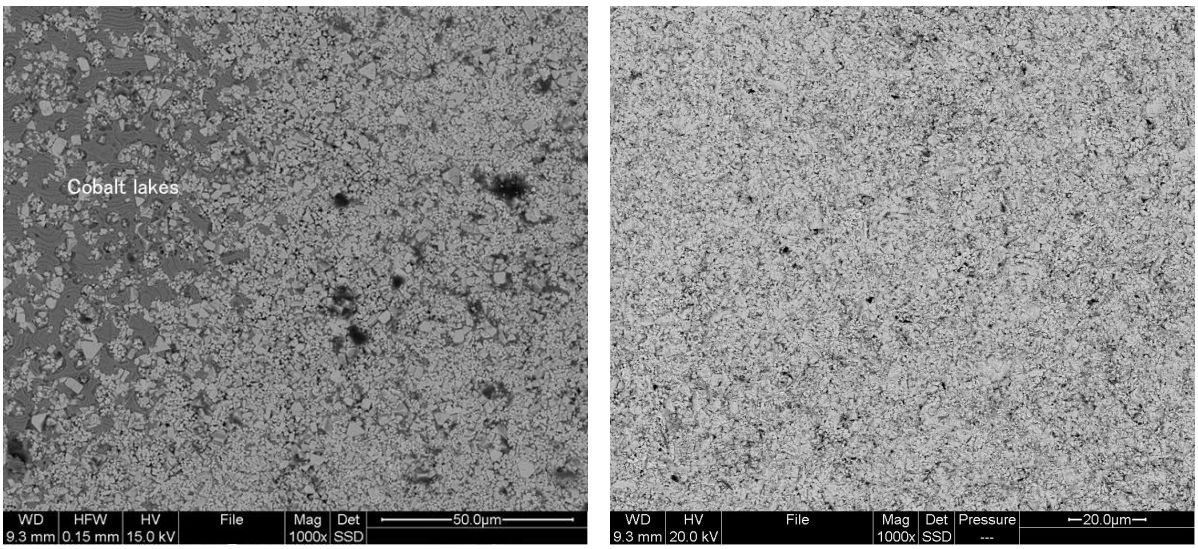

(a) (b)

Figure 4.5: SEM images (BSE) with elemental contrast of the cemented carbides a) WC2 and b) WC2G

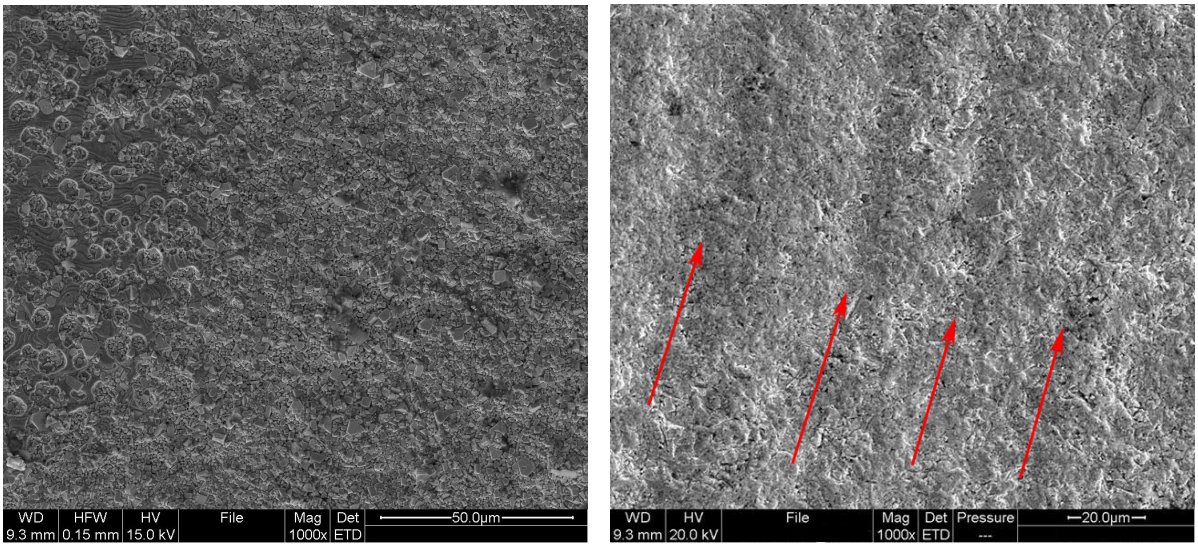

(a) (b)

Figure 4.6: SEM images (SE) with topographical contrast of the cemented carbides a) WC2 and b) WC2G

At higher magnification the difference between WC2 and WC2G can be seen even more clearly (see figure 4.7(a) and 4.7(b)). In case of the unprocessed cemented carbide WC2 the WC grains are showing no defects or remarkable features and the binder phase (Co) can be seen(see figure 4.7(a)). All of the grains possess sharp edges.

Also at this magnification the binder phase is not visible for the ground specimen (see

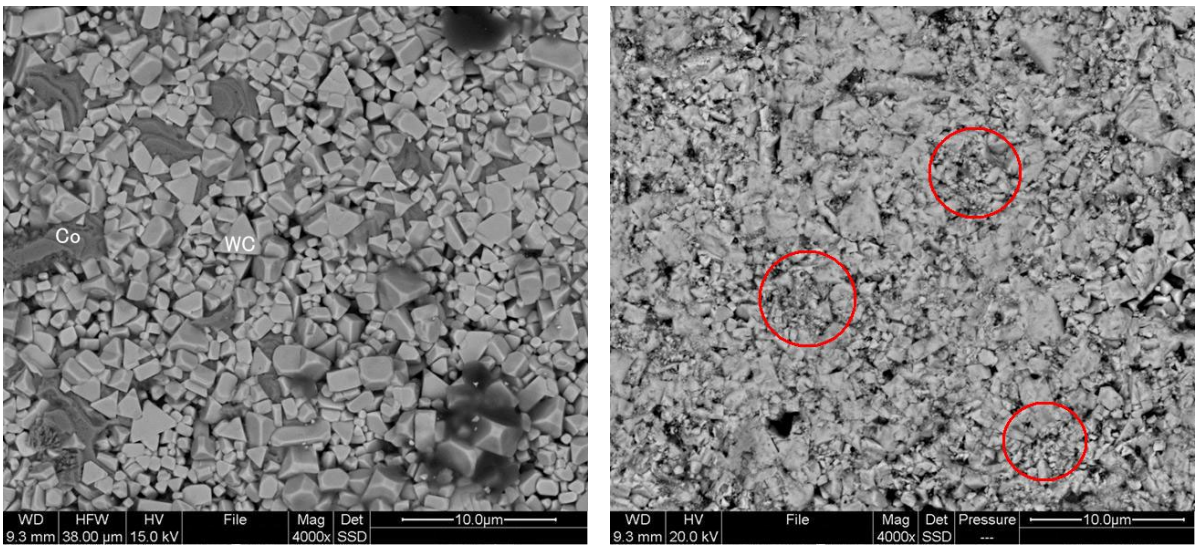

(a) (b)

Figure 4.7: SEM images (BSE) with elemental contrast of the cemented carbides a) WC2 and b) WC2G

figure 4.7(b)). The edges of the WC grains are rounded. On the surface some areas with significantly smaller grains are observable (marked areas in figure 4.7(b)). These are fractures of WC particles and they get embedded in sinks which was also reported in other studies [46, 54, 61, 77]. Because of the size and the gathering of the debris it can be excepted that these particles are just the remaining part of WC grains which were located at the top of the surface. The obtained material contrast shows black areas between the WC grains which indicates holes or areas with low Co content. To ascertain this conclusion further investigations are required.

4.2.2 AFM

As a next step AFM measurements were performed to obtain a three-dimensional surface information and to receive roughness values of the sinter raw and ground specimen surface. An advantage over the SEM is the fact that AFM measurements provide topographical data of the specimen where SEM meausurements just can give a two-dimensional image.

These measurements were done for the WC2 and WC2G material. For the interpretation of these images the intensity bar is defining the colour which is correlated to a height (topographical contrast).

The AFM measurements were performed on a Veeco Dimension 3100 AFM / SPM and the obtained data were analysed with the NanoScope v720r1 Analysis software.

Material: WC2

As seen before in the SEM images the cemented carbide with the coarser grains WC2 has two different representative areas (see figure 4.8(a) and 4.8(b)). With the recorded

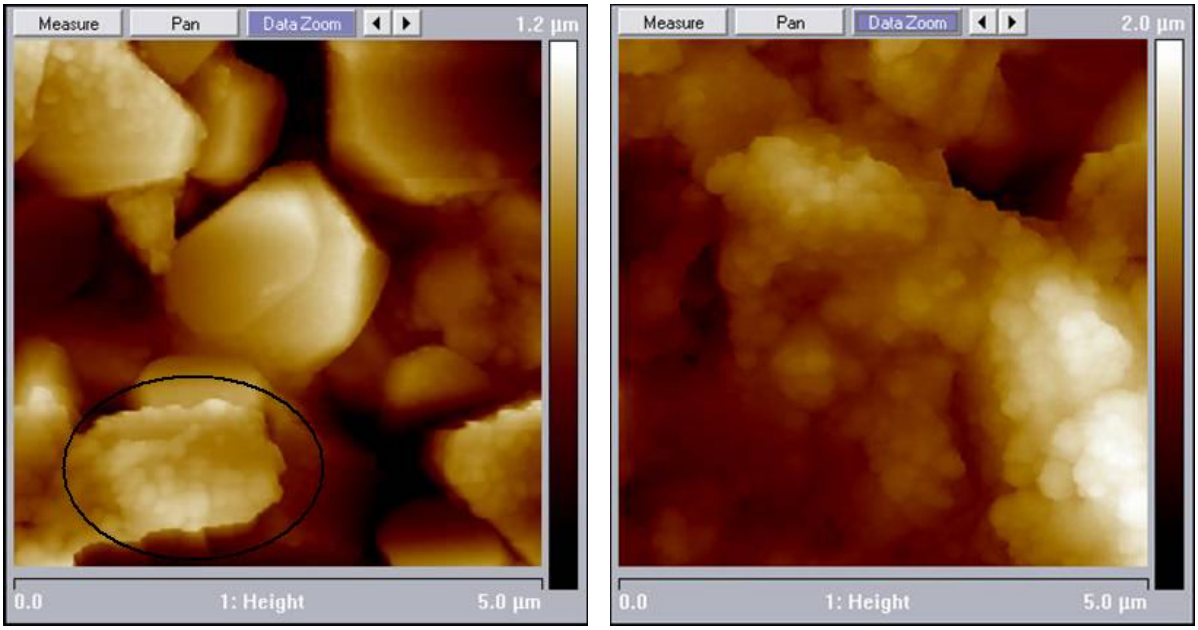

(a) (b)

Figure 4.8: AFM images of WC2; a) tungsten carbide area (WC) b) binder phase area (Co)

data it is possible to perform a 3D-reconstruction (see figure 4.9(a) and 4.9(b)). The images 4.8(a) and 4.9(a) are representing the areas with WC grains at the surface. All of the grains have sharp edges which matches with the SEM results. Some of the WC grains are covered by a foamy layer (marked area in figure 4.8(a))which is the binder phase.

The images 4.8(b) and 4.9(b) are representing the pure binder phase areas (Co). As mentioned before the structure is foam like and there are no sharp edges or transitions within these areas. This feature could not be seen within the SEM results.

Roughness analyses were done on an area of 10 µm x 10 µm to provide representative results (see table 4.2). R_a is the average roughness of absolute values and R_{max} is the

Table 4.2: Evaluated roughness values of the sinter raw cemented carbide WC2

Material	Grain size µm	R_a nm	R_{max} nm
WC2	2,5	251	2244

maximum roughness.

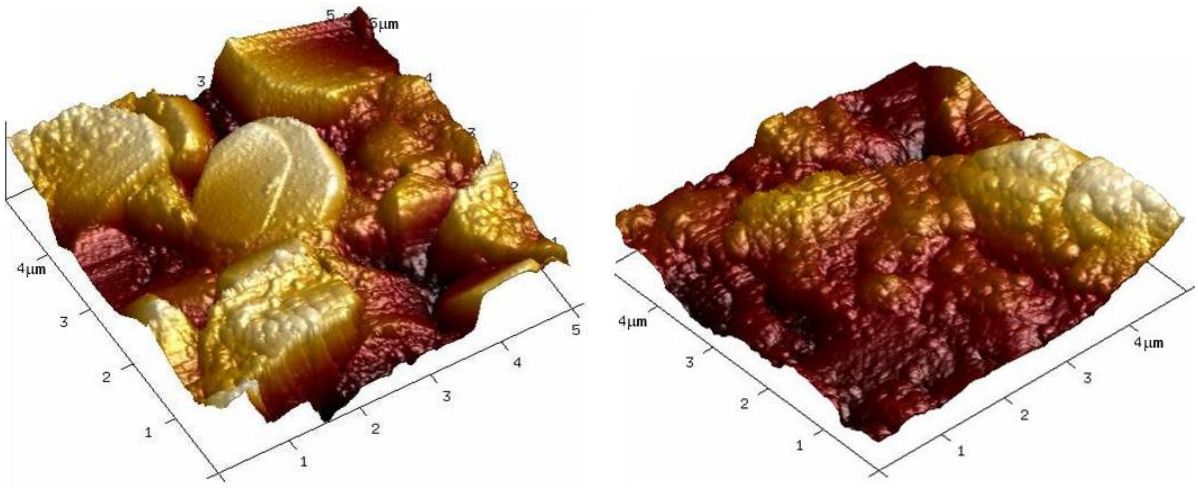

(a) (b)

Figure 4.9: AFM 3D-reconstruction of WC2; a) tungsten carbide area (WC) b) binder phase area (Co)

The average roughness is the sum of the absolute values of all the areas above and below the mean line divided by the sampling length and the maximum roughness is the highest measured peak to valley distance in the profile. From the values in table 4.2 it can be seen that R_{max} has the order of the grain size of the cemented carbide (approximately 2,5 µm).

Material: WC2G

In case of the ground cemented carbide WC2G different results were observed (see figure 4.10(a) and 4.10(b)). It can be seen that the WC grains do not show anylonger sharp edges. The structure of these grains is rounded and the transitions are smooth. Also a lot of smaller grains, which distributed mostly in sinks, can be seen. All of these features are matching the SEM results.

After grinding the cemented carbide the tungsten carbide grains feature round structures and fragments of these get embedded on the surface. These debris grains have a size of about $d = 200\,\text{nm}$ which is quite remarkable compared to the original grain size of 2,5 µm. Again roughness measurements were done on an area of 10 µm x 10 µm (see table 4.3). Compared to the values from sample WC2 (see table 4.2) all roughness

Table 4.3: Evaluated roughness values of the smoothed cemented carbide WC2G

Material	Grain size µm	R_a nm	R_{max} nm
WC2G	2,5	133	1024

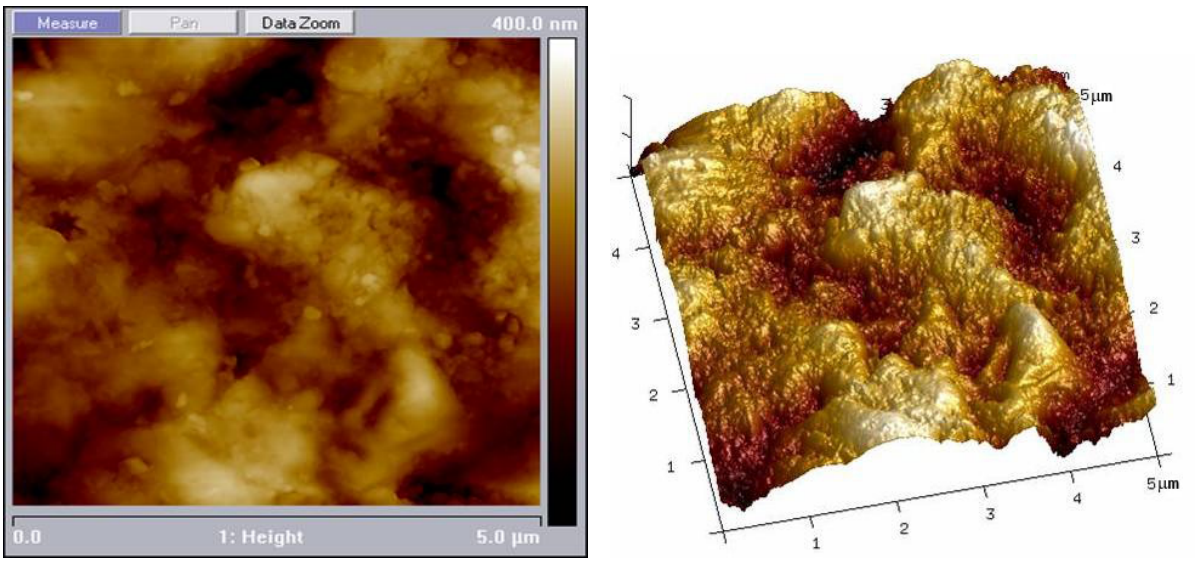

(a) (b)

Figure 4.10: AFM image and 3D-reconstruction of WC2G; a) AFM image (WC) b) 3D-reconstruction

results decreased about the half as expected. A clear conclusion that there is no or less binder phase (Co) present can not be drawn from these results because it is not possible to distinguish the binder from the tungsten carbide.

4.2.3 XRD

Another method for analysing the surface and subsurface of a crystalline material is X-ray diffraction. It can be used to determine strain levels in materials and crystal sizes (see section 3.1.3). These measurements were done for the WC2 and WC2G material.

The XRD-measurements were performed on a Siemens D501 in Bragg-Brentano geometry and the obtained data were analysed with the DIFFRAC.EVA software.

Material: WC2 and WC2G

$\theta/2\theta$-scans were performed for the samples WC2 and WC2G from 25° to 80° and the recording time was $t = 0{,}02\,\mathrm{s}$ per 0,02° step. In figure 4.2.3 the measured XRD spectra of WC2 (red line) and WC2G (black line) is shown. In both spectra the background signal was substracted and the curves were smoothed with algorithms available in the software.

The detected peaks were identified as tungsten carbide with hexagonal crystal structure and lattice parameters of $a = b = 2{,}90631$ Å and $c = 2{,}83754$ Å. In comparison of these two recorded spectra it can be seen that line broadening is appearing in the processed cemented carbide WC2G and also that the intensity of the received signal is lower (see close up in figure 4.2.3). To analyse the strain density a Williamson Hall

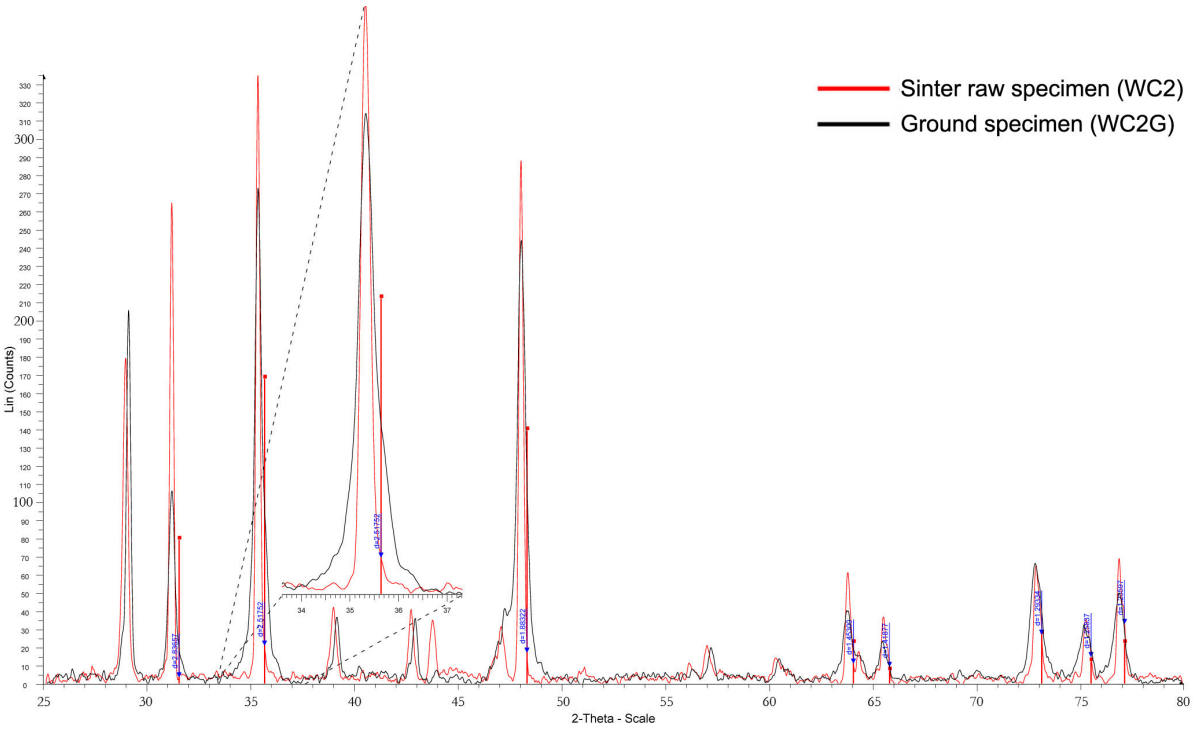

Figure 4.11: XRD profiles of the cemented carbide WC2 and WC2G with one peak as a close up

plot was created (see equation 3.2). Because the sinter raw WC2 and the ground cemented carbide WC2G were measured in the same device and due to the fact, that just a comparison is made between these hard metals, the instrumental broadening can be neglected. For obtaining figure 4.12 the „modified“ Williamson Hall plot was calculated from the integral breadth. If the slope of both cemented carbides is considered, the ground sample WC2G has about a 263% higher inhomogeneous lattice strain than the sinter raw material. This means that the grinding process is inducing strains into the lattice of the cemented carbide. To determine the sampling depth of the XRD analysis the mass absorption coefficient μ for WC ($\mu = 161{,}78\,\mathrm{cm}^2/\mathrm{g}$) and the Lambert-Beer Law is needed

$$I = I_0 e^{-\mu z} \tag{4.1}$$

which describes the intensity relation between the diffracted beam I and the incident beam I_0. z is the distance covered by the diffracted beam in the material. For example the sampling depth of the WC(100) peak at a bragg angle of $\theta = 17{,}8°$ is $d = 1{,}5\,\mu\mathrm{m}$ [78]. Overall it is worth noting that the depth of XRD analysis is approximately $d = 1{,}5\,\mu\mathrm{m}$ in the 2θ region from 30° to 55° [79].

The intercept of the linear fit offers information about the crystallite size, but the use of this broadening due to crystallite size is generally limited to cases where the average size is $\leq 1\,\mu\mathrm{m}$ [80]. However, it can be noted that the intercept of the ground

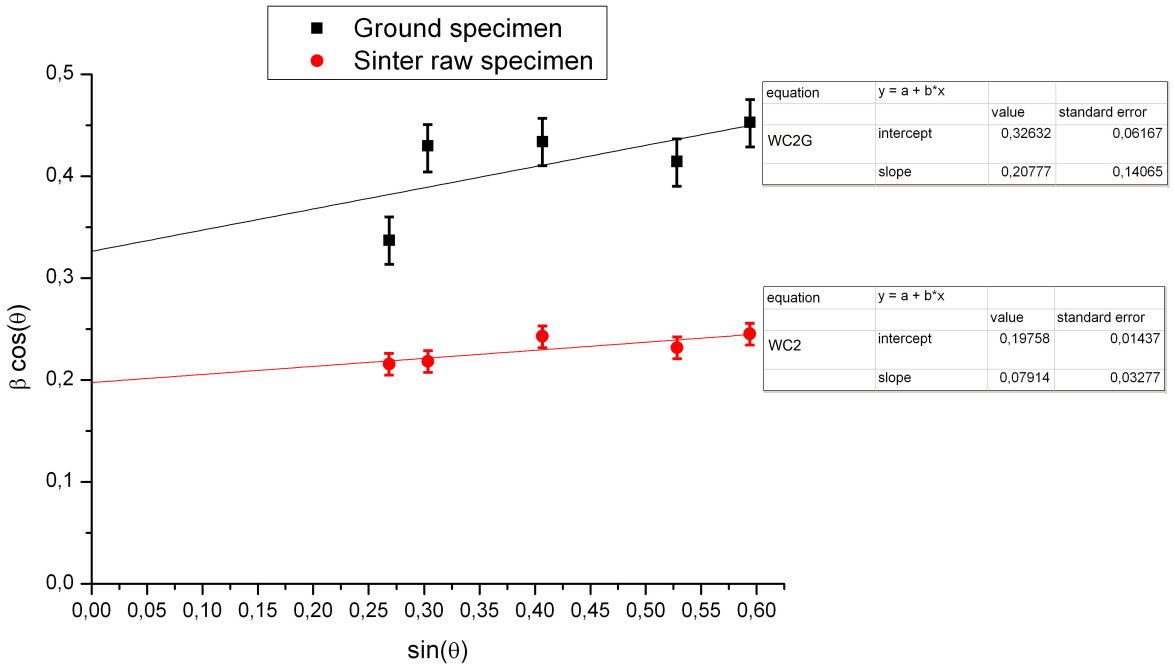

Figure 4.12: Williamson Hall plot of the cemented carbide WC2 and WC2G

cemented carbide WC2G is increasing in comparsion to the sinter raw WC2. This would corresponds to a decrease of the average crystallite size at the surface and subsurface because most of the signal information originates from a depth of around $d = 1{,}5\,\mu m$. The decrease of the average crystallite size from XRD investigation confirmes the surface results from SEM and AFM. There small debris which is covering the surface can be seen. Information about the grain size in the subsurface regions will be given in the cross-section analysis chapter (see following chapter).

4.3 Cross-Section Analysis

As a next step cross-section investigation were performed with different devices and different preparation techniques (SEM, TEM). Cross-section measurements require specimen preparation, which is a destructive method and could affect the specimen. So the obtained results should be analyzed with care.

4.3.1 SEM

Instead of mechanical polishing all specimen were prepared by an argon ion beam (see section 3.2). Cross-section preparation was done with the Gatan *Ilion*$^{+\text{TM}}$ Model 693. To prevent re-deposition the polishing was performed from the bulk towards the surface. Also a shoot out of material (especially Co) at the surface can be prevented with this

polishing direction. Because the specimen has a thickness of around $d = 250\,\mu m$, the polishing time at an accelerating voltage of $U = 4\,kV$ was about $t = 24\,h$.

An important issue of this specimen preparation technique is known as „curtaining effect“. This effect consists of the formation of striations across the polished area and originates of different chemical compositions or uneven topography of the specimen. In case of the cemented carbide the WC grains often cause this „curtaining effect“ because of their high hardness. Co is much softer and therefore it is favoured during polishing. The thicker the cross section is, the more distinct this „curtaining effect“ gets. To reduce the „curtaining“ effect the polishing time or the accelerating voltage can be increased. In case of the cemented carbide a significant reduction of this effect is not possible.

The SEM measurements were performed on a FEI ESEM Quanta 600 FEG and the obtained data were analysed with the xT microscope control software.

Material: WC1 and WC1G

The obtained cross-section images of the cemented carbide specimens with finer grain size can be seen in figure 4.13(a) and 4.13(b). The surface of WC1 and WC1G illustrates

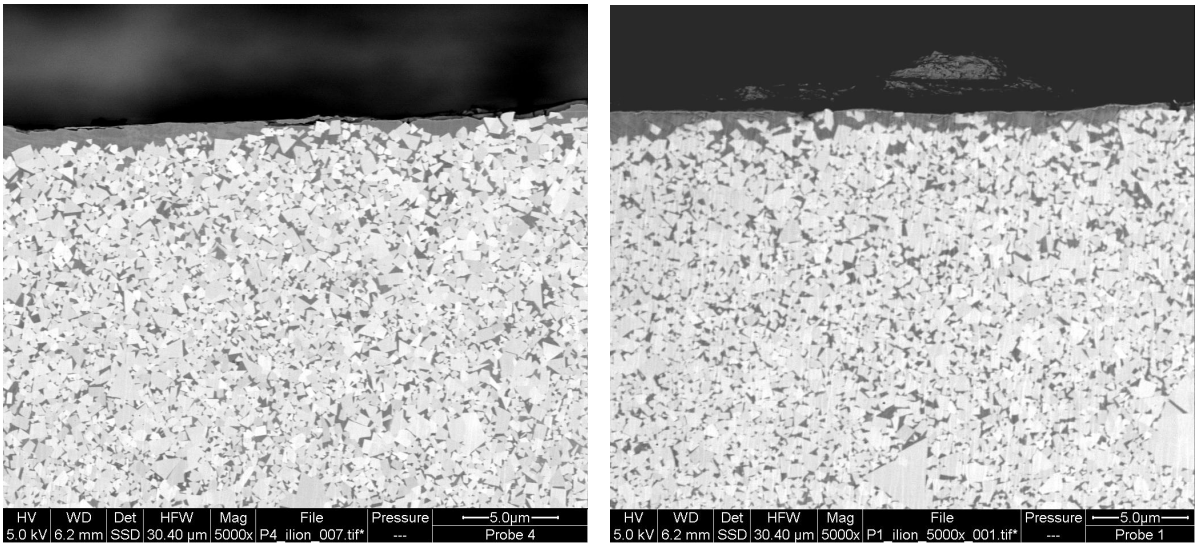

(a) (b)

Figure 4.13: SEM images (BSE) of cross-section samples of a) WC1 and b) WC1G

at this magnification to be the same. Both are showing areas of binder phase at the surface and some areas where the WC grains are at the top. It can be confirmed that the average grain size of these cemented carbides is $0,6\,\mu m$. Also at higher magnification no differences can be seen (see figure 4.14(a) and 4.14(b)). The WC grains do not show any deformation and no grinding grooves can be seen. These results match with the obtained surface results (see section 4.2.1).

From the foregoing it follows that the cemented carbides WC1 and WC1G are showing no difference and they match in each feature. As confirmed later with the manufacturer

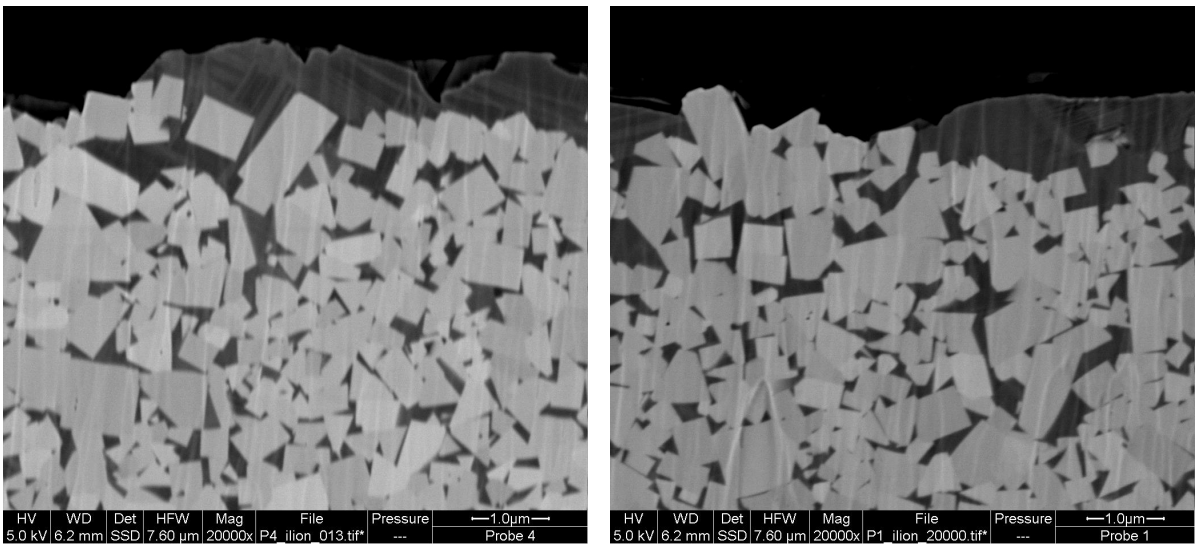

(a) (b)

Figure 4.14: SEM images (BSE) of cross-section samples of a) WC1 and b) WC1G

WC1G actually had no ground surface and was the same sample as WC1.

Material: WC2 and WC2G

For the samples WC2 and WC2G with the coarser grains images at the same magnification were acquired (see figure 4.15(a) and 4.15(b)). Both specimens were prepared using the same technique and the same parameters. In the image of WC2 it can be seen that

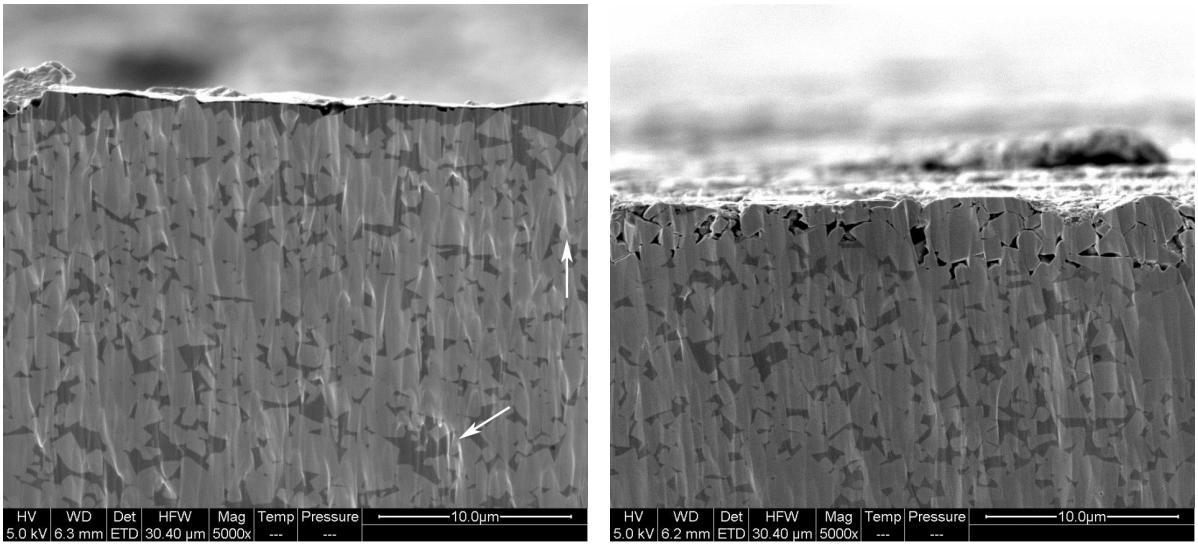

(a) (b)

Figure 4.15: SEM images (SE) of cross-section samples of a) WC2 and b) WC2G

the surface consists again of areas with binder phase and some areas with WC grains on top, as for the cemented carbide WC1. Also the curtain effect, which originates from preparation, can be seen all over the cross section (for example marked areas with white arrows see figure 4.15(a)).

In case of WC2G the surface is showing no binder phase covered areas. The surface is composed of WC grains of different size and at the subsurface a depletion of the binder phase can be seen. Whether the binder phase is totally removed can not be judged from these images. Also regions with clusters of small grains can be seen. To differentiate these features images at higher magnification were acquired (see figure 4.16(a) and 4.16(b)). Image 4.16(a) from the sinter raw cemented carbide confirms the previous results. The

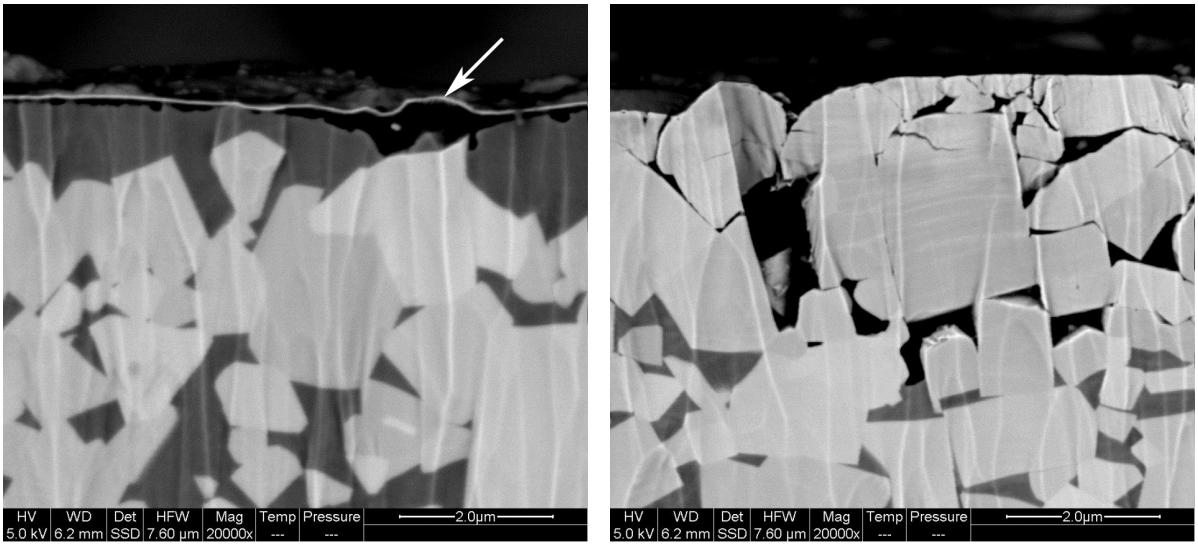

(a) (b)

Figure 4.16: SEM images (BSE) of cross-section samples of a) WC2 and b) WC2G

thin layer (arrow in figure 4.16(a)), which covers the binder phase and the WC grains results from a sputter process and can be neglected.

At higher magnification a lot of features can be seen for the ground specimen WC2G. Therefore this features are going to be numbered in figure 4.17 and explained below. Additional cracks in the WC grains (white arrows in figure 4.17) and again fragments (number 2 in figure 4.17) can be identified in the cemented carbide WC2G. Cracks can be seen even in deeper regions way below the surface (white arrow with number 1 in figure 4.17). Areas close to the surface have a brittle appearance (marked area 2 in figure 4.17). The fragments occur mostly close to the surface and there are two possible ways to explain this circumstance. Re-embedding of fragments in the material can occur during further contact of debris with the surface or the binder phase gets extruded or pushed out through the network of cracks that is formed in the WC grains [46, 59, 60]. Which mechanism happened here is not fully clear. To analyse these areas more precisely an analytical TEM investigation was necessary (see section 4.3.2).

As already mentioned the binder phase can be pushed out through a network of cracks

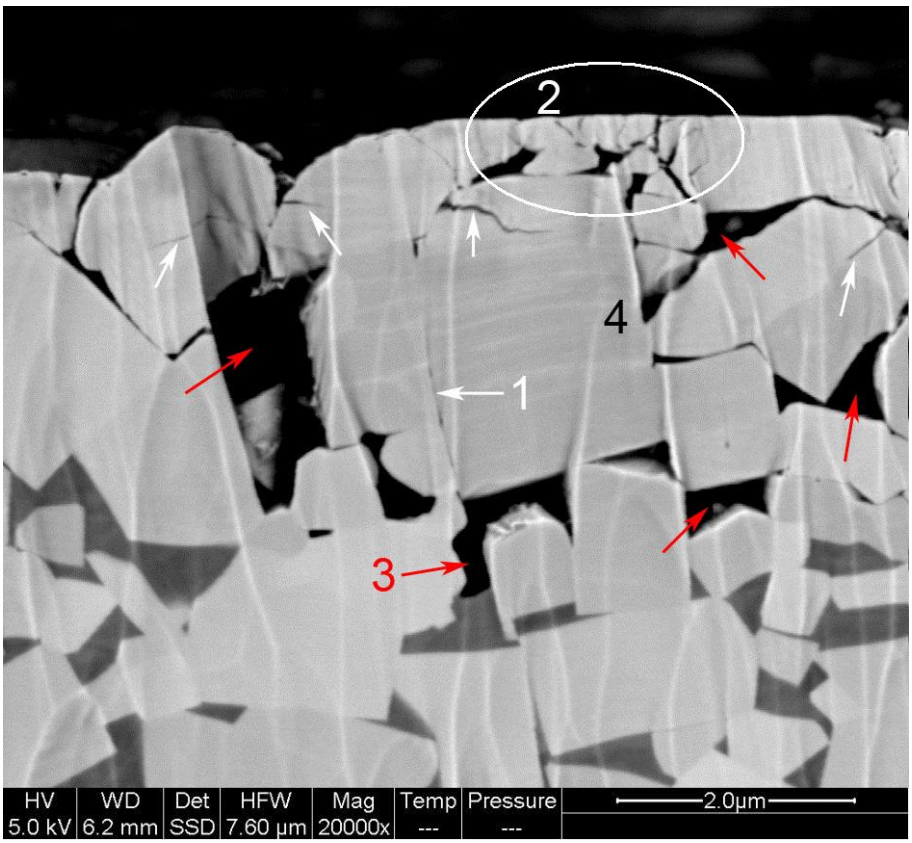

Figure 4.17: SEM cross section of specimen WC2G (close up of figure 4.16(b))

in the WC grains. This mechanism supports an observed formation of Co containing layer on the surface after wear tests in previous studies. This layer is called tribofilm and consits of small fragments of WC grains and some binder phase [54, 61, 62]. This would explain why these brittle areas are still held at the surface. Tribofilms were not be seen in SEM investigations. Therefore a TEM investigation is necessary to ensure if there is any tribofilm present.

At higher magnification it can be seen that the depletion of binder phase is distinct over a wide area at the subsurface of the cemented carbide WC2G (red arrows in figure 4.17). The depletion takes place until a maximum depth of $d_{max} = 4{,}3\,\mu m$ (red arrow with number 3 in figure 4.17). Averaged over a distance of 30 µm the depletion depth amounts to $d_a = 2{,}8\,\mu m$. This extrusion or removal of binder phase was also discovered in previous studies of different wear tests [37, 59–61, 81, 82]. As already mentioned the binder phase depletion takes place via a network of cracks formed by a combination of plastic deformation (micro cracks) and micro-abrasion [51]. It could be possible that the extrusion of binder is favoured during the grinding because a metallic emulsion is used as a coolant, which is chemically reactive to the binder. But also in previous dry sliding studies an extrusion of binder phase was observed [37,61]. In image 4.16(b) another type of plastic deformation is present, slip lines (number 4 in figure 4.17). This deformation also was reported in previous studies of wear in tungsten carbide [54].

4.3.2 TEM

To receive more detailed informations TEM investigations were performed at even higher magnification. The most difficult part for TEM investigations is the specimen preparation which is time-consuming and not always successful (see section 3.2). Several techniques were tried:

- Plan view preparation,
- Sandwich cross-section preparation and
- FIB preparation.

The TEM measurements were performed on a Philips CM 20 with a LaB_6 as an electron source and on a FEI Tecnai F20 with a field emission gun with a monochromator additionally equipped with an external scan unit (Digiscan II). The Philips CM 20 uses a Noran high purity Germanium (HPGe) EDX detector with ultrathin window, which is able to detect elements from $Z > 6$ (qualitatively and quantitatively). X-ray spectra were acquired and processed using NORAN System Six (NSS).The FEI Tecnai F20 uses a EDAX Saphire Si(Li) detector and EFTEM analysis were performed with the high resolution GIF. All obtained data were analysed by using DigitalMicrograph™ (GMS 2.1).

Plan View

In case of the plan view preparation several attempts were necesseray and for all specimens electron transparent areas could be obtained. All specimen were mechanically ground and dimpled from the bulk side to keep the surface side unaffected.

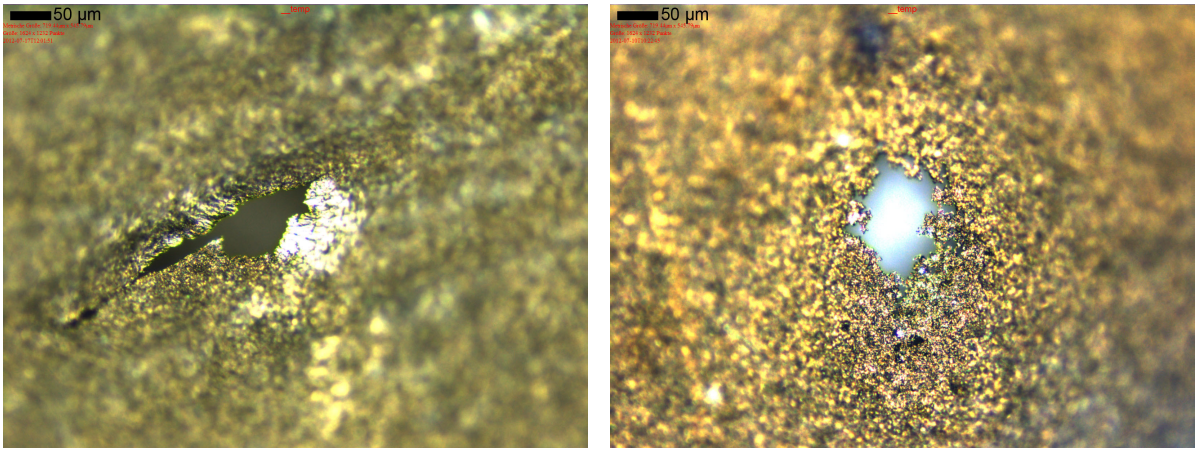

(a) (b)

Figure 4.18: Optical microscope images at 20x magnification of the plan view prepared specimen a) WC2 b) WC2G

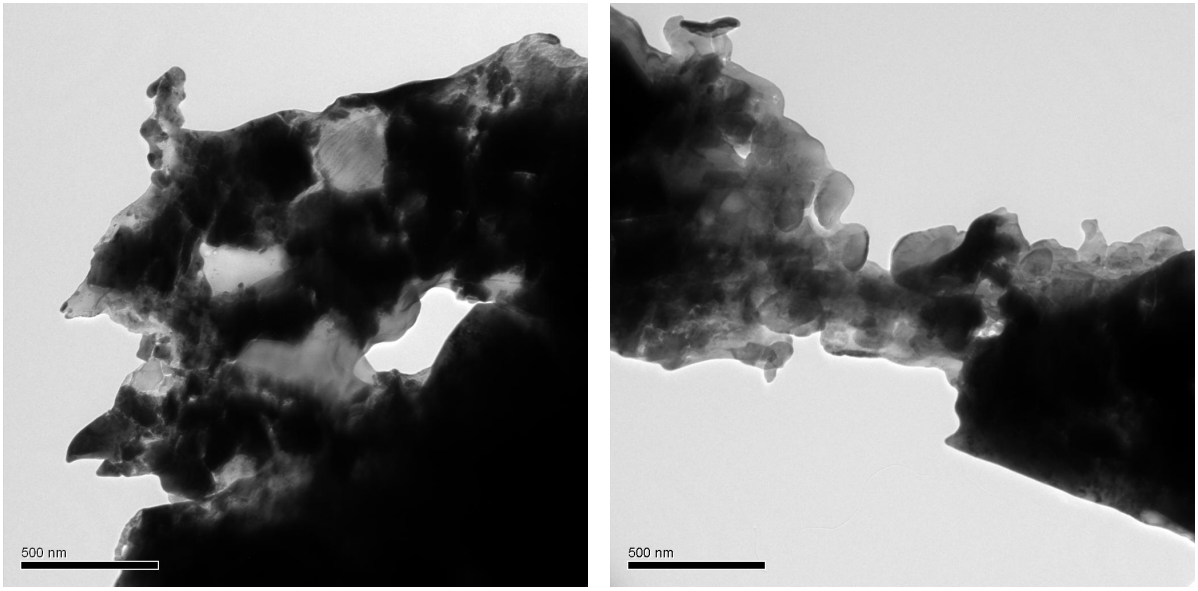

(a) (b)

Figure 4.19: TEM BF images of the plan view prepared specimen a) WC2 b) WC2G

The technique itself is quite easy and the preparation of the specimen is finished fast (about $t = 8 - 10\,\mathrm{h}$)(see figure 4.18(a) and 4.18(b)). But the fact that in TEM it is just possible to observe and research areas with a thickness of only a few tens of nanometers it is not possible to receive representative „cross-sections“(see figure 4.19(a) and 4.19(b)). In case of the sinter raw specimen WC2 it could be possible that just the Co, which is covering the surface, can be seen because just a few WC grains are at the top of the surface. It can be noted that the structures in image 4.19(b) of WC2G look like the results out of literature (see figure 2.10(b)). Compared to the SEM results of the depth of damage this circumstance let to foresee further investigations with this preparation technique.

Sandwich Cross-Section

The sandwich cross-section preparation with a dimpler and ion milling (see section 3.2) was much more difficult and time-consuming (about $t = 16 - 20\,\mathrm{h}$). For the successfully prepared specimen it was found out that the investigatable electron transparent areas are much too far away from the original surface area of the specimen (see figure 4.20(a) and 4.20(b)) and the transparent areas are to small. At the maximum an investigatable area with a width of about 250 nm was achieved (see figure 4.21(a) and 4.21(b)). This is just half of the finest WC grain size. A reason for the narrow electron transparent band could be the brittle structure close to the surface. While ion milling this brittle structures get thin and unstable and fall apart. Because of these issues this preparation technique seems to be not a recommendable approach for the required investigation of the surface region of the specimens.

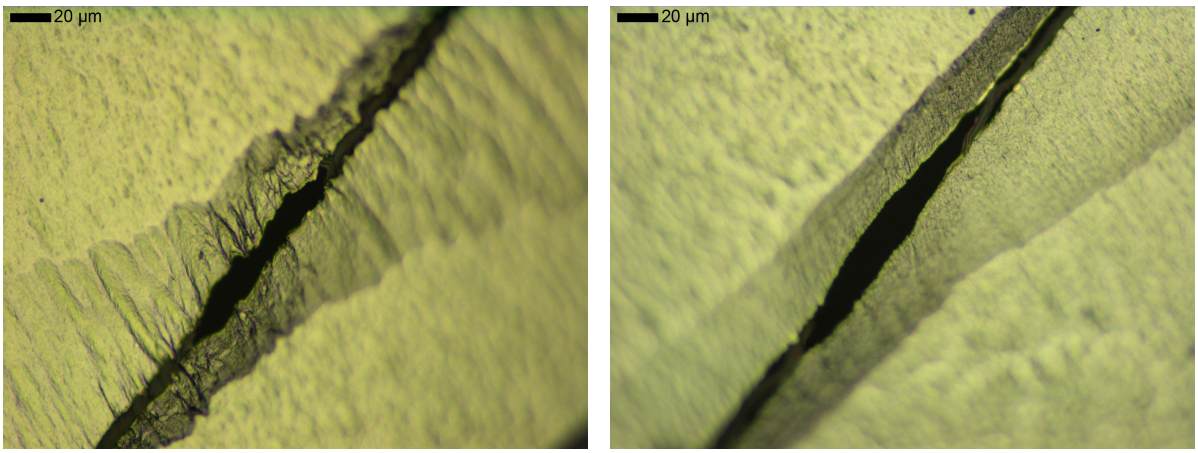

(a) (b)

Figure 4.20: Optical microscope images at 50x magnification of the sandwich cross section prepared specimen a) WC1 b) WC1G

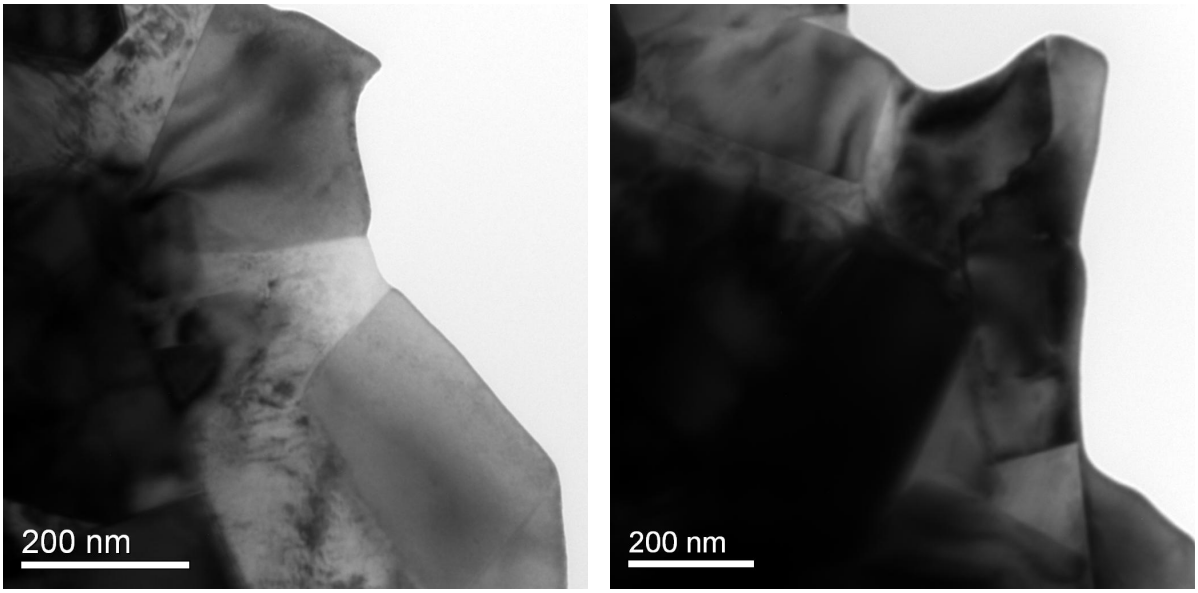

(a) (b)

Figure 4.21: TEM BF images of the sandwich cross section prepared specimen a) WC1 b) WC1G

FIB-Lamella

It became apparent that preparing a lamella via FIB shows the best results. The FIB TEM specimen preparation is quite time-consuming, but highly successful. Electron transparent areas up to several µm are reached, which is in comparsion to conventional methods a huge advantage. However, considering the results obtained via SEM cross-sections, this method offers the possibility to extract a TEM sample from a selected

region of interest to verify and refine the information gathered so far with additional techniques with higher resolution and analytical capabilities.

Material: WC2G

The advantage of the FIB preparation is that the surface of the specimen can be observed first via SEM to precisely determine the area of interest. In the SEM image 4.22(a) the

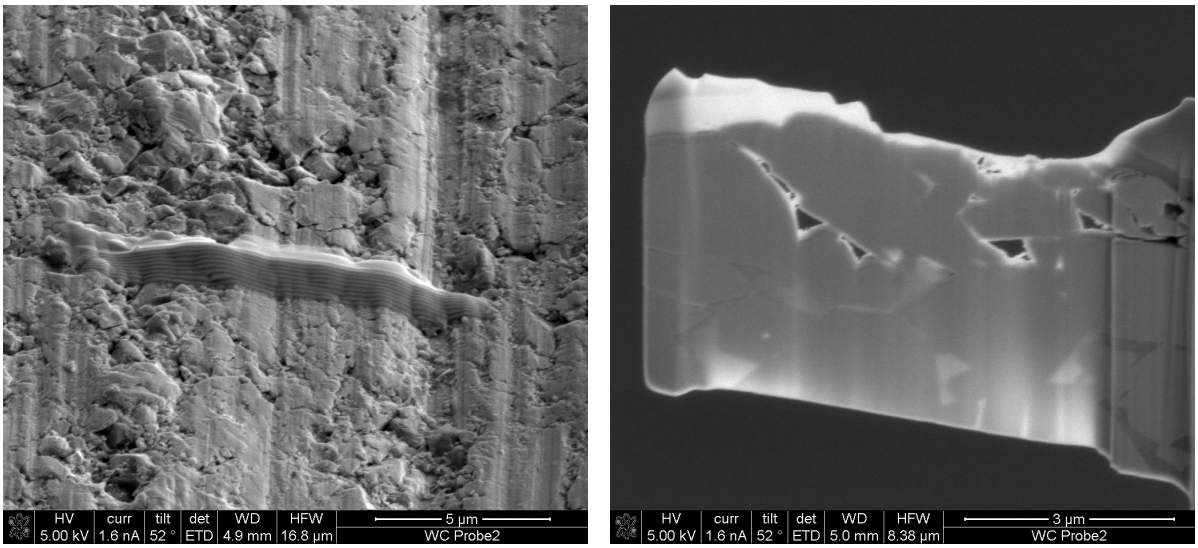

(a) (b)

Figure 4.22: SEM images of the FIB prepared TEM lamella; a) Chosen area for the lamella b) Lifted out lamella before thinning

chosen area, which is already covered with platinum as a protection, can be seen. Based on the information about specimen stability gained in the preceding investigations the lamella was prepared more wedge like with the thicker area close to the specimen surface. This should prevent that the lamella is falling apart because of the brittle structure of the subsurface. After the lift out the lamella is fixed onto a copper grid and thinned to electron transparency (see figure 4.22(b)). The result can be seen in the HAADF image 4.23(a) done with FEI Tecnai F20 in STEM mode. The lamella is upside down in figure 4.23(a) as indicated, therefore the surface region is at the bottom of the image. At the right lower edge of the lamella some residual platinum can be seen, which originally covered the whole surface. The bright areas in the lamella are representing WC grains and the darker areas the binder phase Co (labeled areas in figure 4.23(a)). In the immediate subsurface region the WC grains are brighter because the lamella is thicker there, hence more electrons get scatterd. The relative thickness map (see figure 4.23(b)) illustrates the thickness variances within the lamella. A thickness value in the region of one mean free path or smaller of the electrons that travel through the specimen is required to perform accurate investigations. This is just true for some areas in the

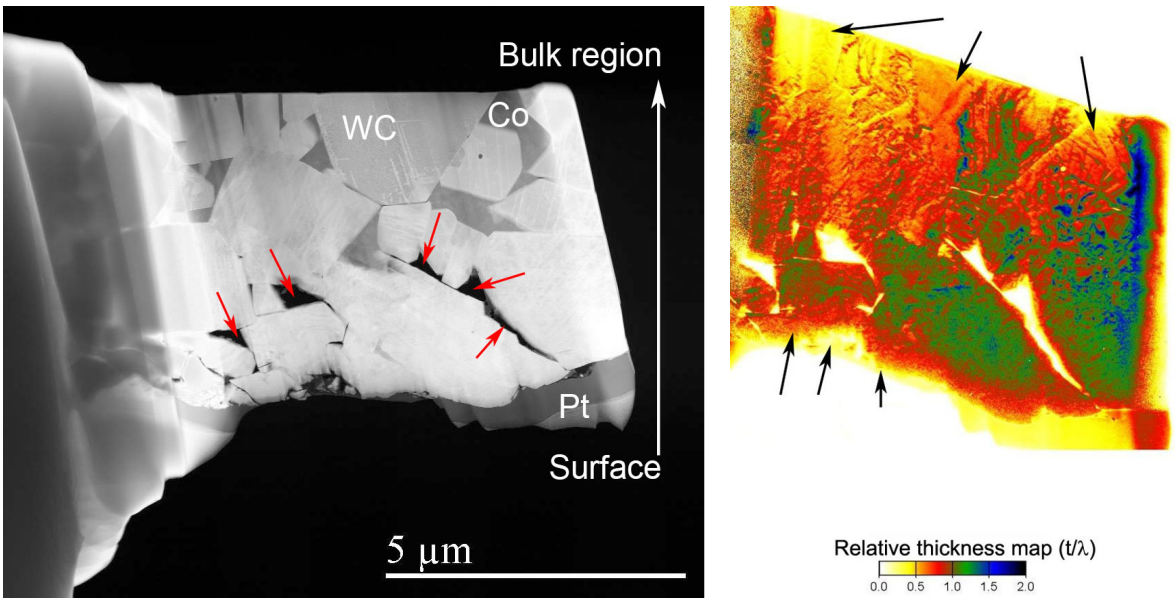

(a) (b)

Figure 4.23: FIB prepared TEM lamella; a) HAADF overview image b) relative thickness map

bulk and surface (arrows in figure 4.23(b)). For the other regions EELS and EFTEM investigations are not viable and post-thinning would be necessary.

In image 4.23(a) it can be seen that the binder phase is totally removed in some regions since the contrast is fully black (red arrows in figure 4.23(a)). Even for some subsurface regions until a depth of $d = 2{,}4\,\mu m$, which is in the order of the WC grain size, the binder is not present anymore. This can be confirmed at higher magnification (see figure 4.24). At the surface debris, resulting from the grinding process as described in the SEM investigation (see section 4.3.1), can be seen (white ellipse in figure 4.24). Two regions were chosen (see labeled positions in figure 4.24) for closer investigation. Positon 1 (see figure 4.25(a)) shows a lot of small debris with a size of about 200 nm. The different contrast in the left half of the image in comparsion to the right half is caused by the varying thickness of the lamella. At the left side the lamella is getting slightly thicker.

Position 2 (see figure 4.25(b)) shows also some debris but not so much as in position 1. There are two possible explanations. Either this spot represents an area where no debris enrichment was taking place or through the thinning of the lamella debris was dropping out. In comparison position 2 is thinner than position 1. Additional micro cracks in the WC grains can be identified. No edges do show sharp transitions, they are rather rounded.

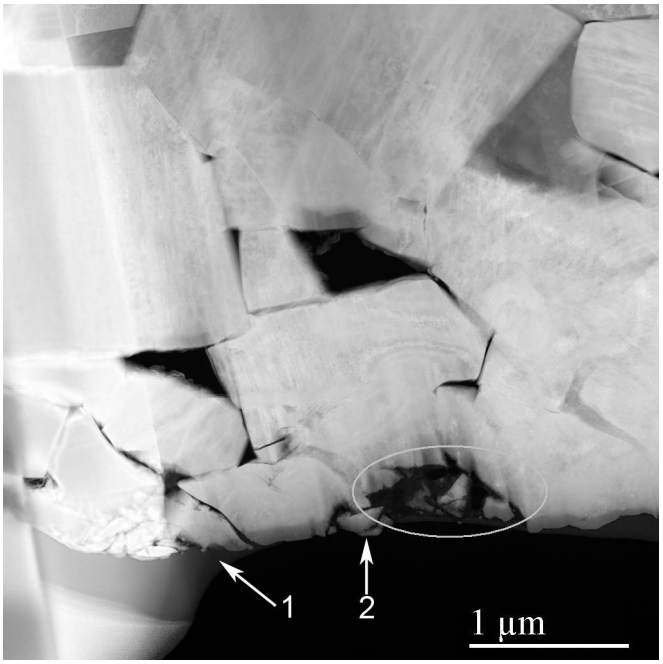

Figure 4.24: HAADF image of the lamella

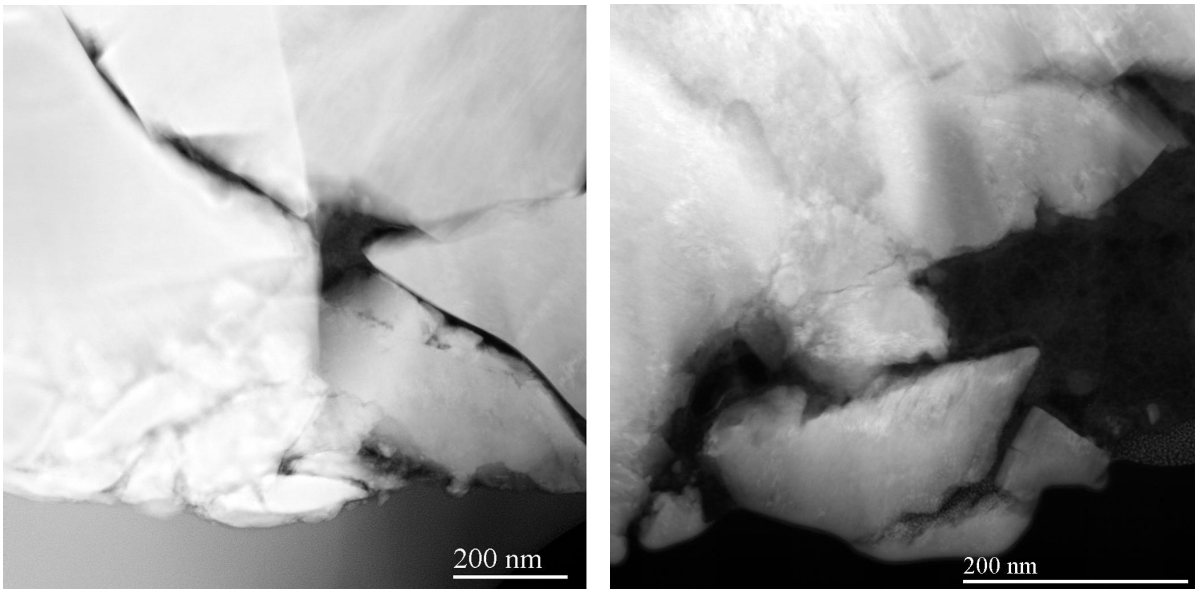

(a) (b)

Figure 4.25: HAADF images; a) position 1 and b) position 2

Same results for position 2 were obtained with the Philips CM 20 in TEM BF mode (see figure 4.26(a) and 4.26(b)). Using BF for imaging shows that the debris is embedded in a thin layer.

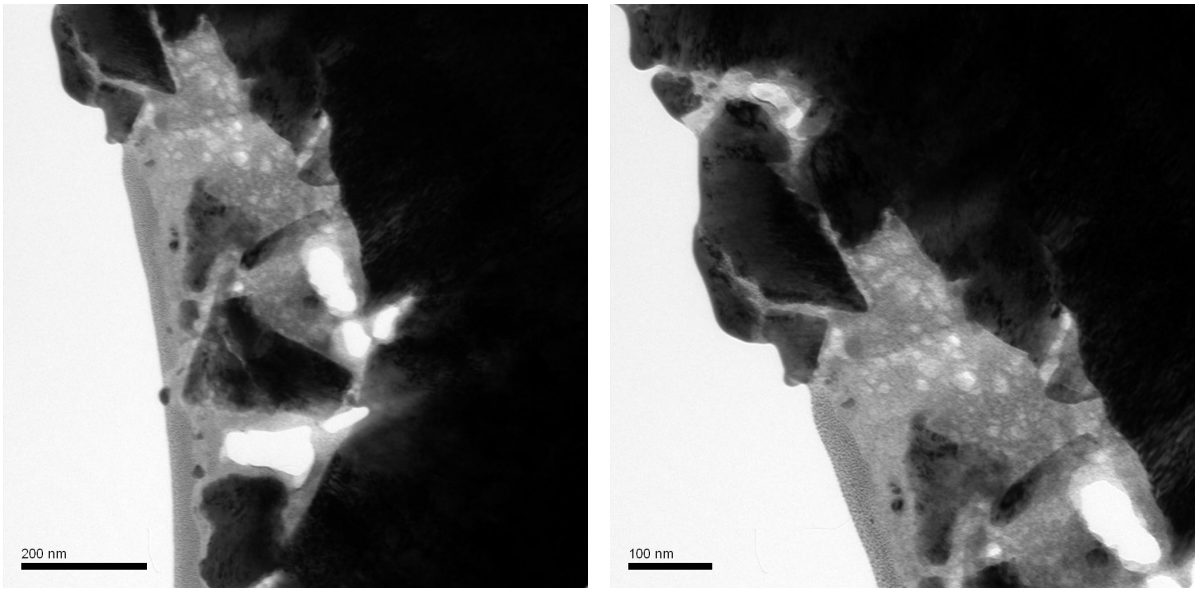

(a) (b)

Figure 4.26: TEM BF images; a) area marked with white ellipse in figure 4.24 and b) position 2

In previous studies of wear with cemented carbide often a tribofilm, which covers the surface, was detected [54,61,62,83]. This tribofilm is formed during grinding or scratching the surface and usually consists of debris from the WC grains and some binder phase. To clarify the circumstance for the ground specimen WC2G STEM EDX analysis was

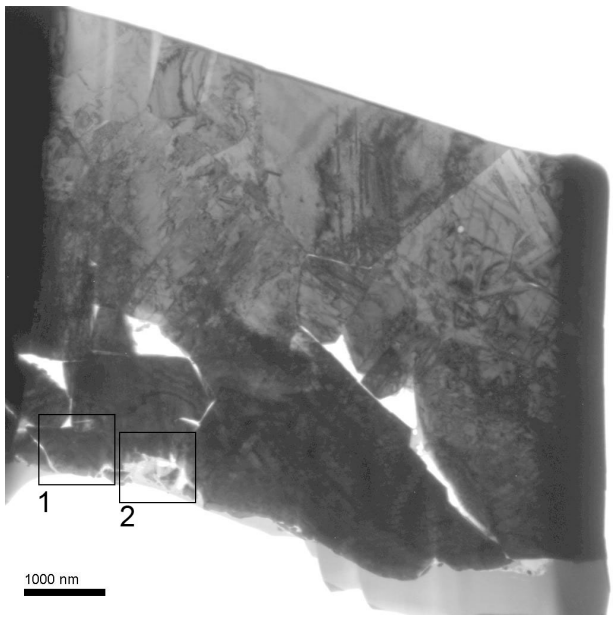

Figure 4.27: TEM BF image with the two labeled areas for STEM-EDX

performed.

An EDX determination of two chosen areas was performed with the Philips CM 20 in STEM mode. The chosen areas are labeled in figure 4.27. For both areas the acquisition time was $t = 30\,\mathrm{s}$ and the results can be seen in figure 4.28 and 4.29. In both spectra

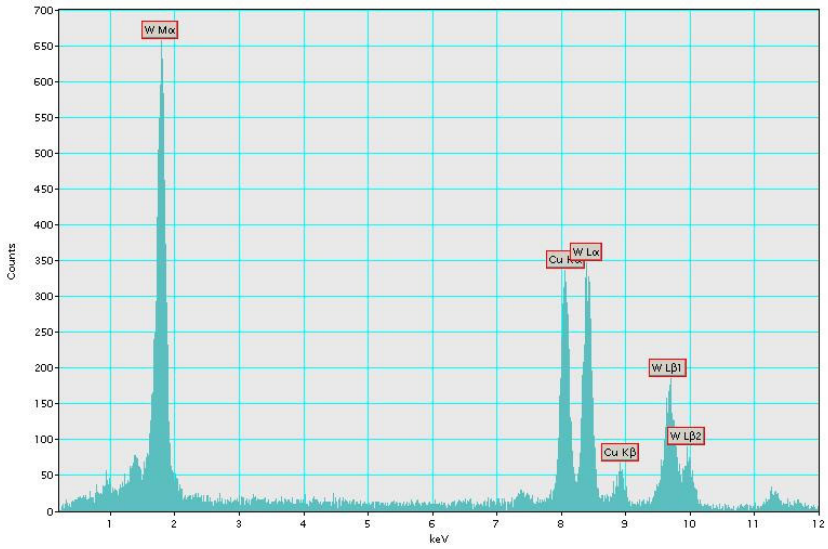

Figure 4.28: STEM-EDX result of area 1

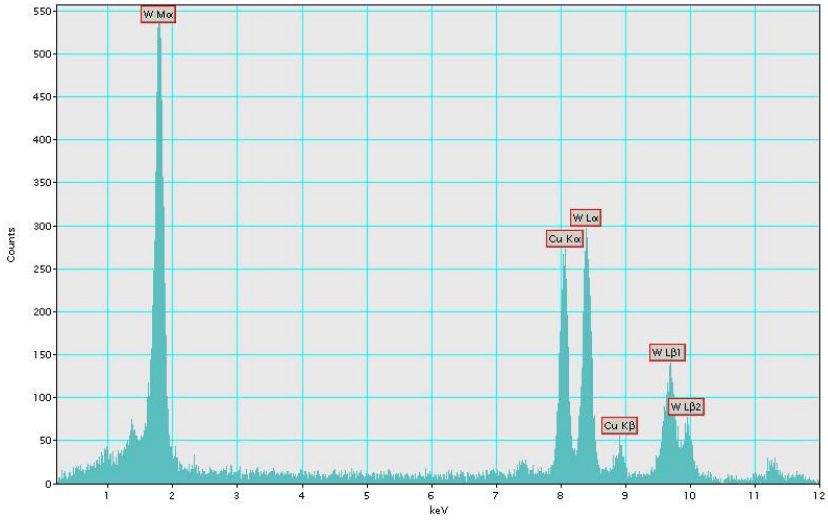

Figure 4.29: STEM-EDX result of area 2

tungsten and copper can be identified, but no cobalt peaks were detected. The copper peaks originate from the copper grid onto which the lamella is fixed. This means that just tungsten can be found in the specimen. In comparison area 1 possesses a higher intensity than area 2 because a thicker area is analysed.

Because the areal STEM EDX analysis did not reveal any binder phase at the surface STEM EDX point analyses were performed. The point EDX spectra were done on the FEI Tecnai F20. For more precise analysis area 2 from figure 4.27 was chosen. Three different spots in this area were selected (see labeled spots in figure 4.30). For all three

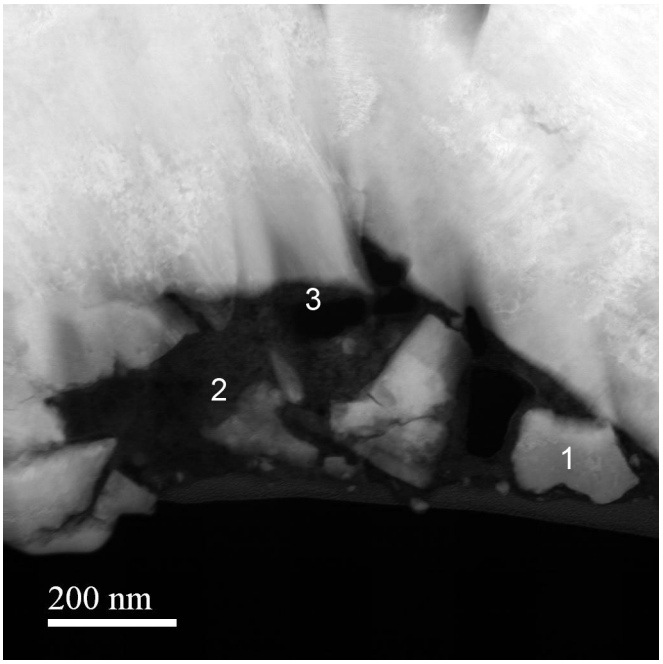

Figure 4.30: HAADF image with the three labeled spots for STEM EDX

spots the acquisition time was $t = 50\,\mathrm{s}$. In figure 4.31 the spectrum for the first spot can be seen. Again copper can be identified which originates from the copper support grid.

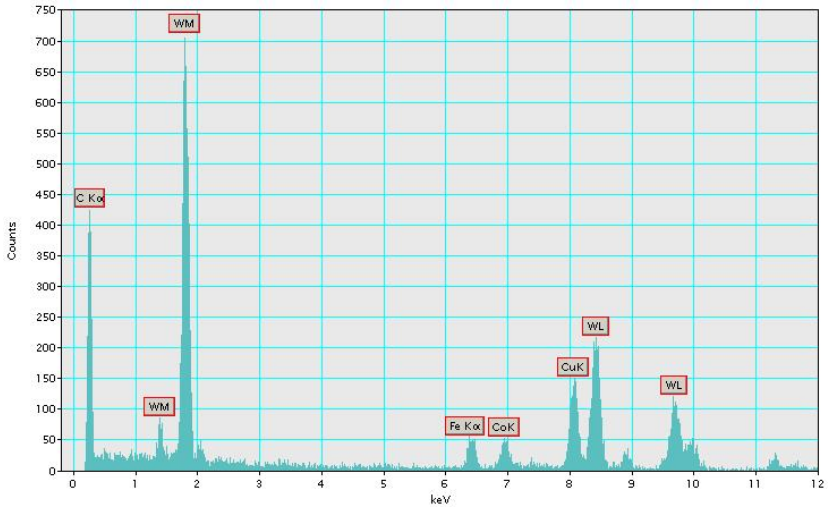

Figure 4.31: STEM-EDX result for spot 1

Tungsten was also identified because spot 1 lies completely on a tungsten carbide debris

grain. The obtained C peak has to be treated carefully because the carbon could also originate from contamination and not from the carbon in the tungsten carbide debris grain. Much more interesting is the fact that some iron and some cobalt was detected. This result has to be treated carefully as well, because in each EDX spectra recorded with the FEI Tecnai F20 Fe and Co peaks can be found. If these two peaks have the same intensity they most likely originate from the objective lens pole pieces of the microscope and can be neglected. In spectrum 4.31 the Fe and Co have the same intensity and therefore they do not originate from the ground cemented carbide WC2G.

The second and third spots are not located on a grain and should give some information about the film which surrounds the grains. In figure 4.32 the X-ray spectrum for the second spot can be seen. Although spot 2 lies not on a tungsten carbide grain a small

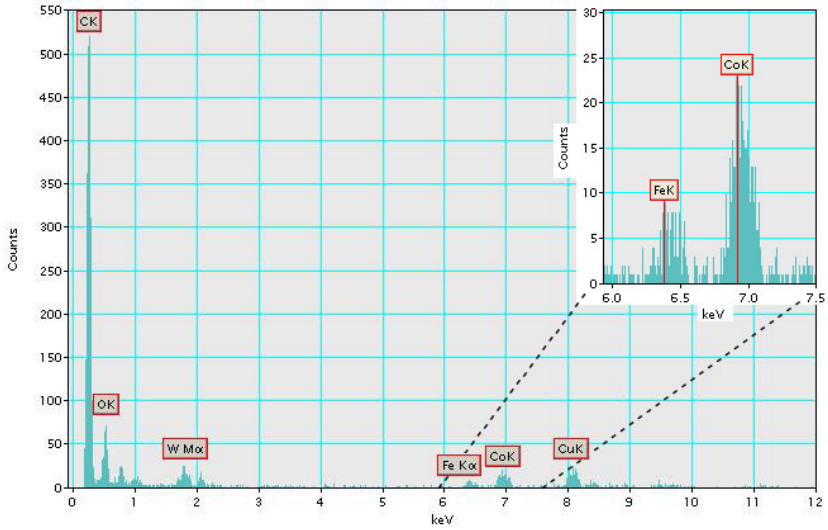

Figure 4.32: STEM-EDX result for spot 2

peak of tungsten can be seen. This signal is caused by stray radiation from neighbouring grains. If the recorded Fe and Co peaks are considered it can be seen that they do not anymore have the same intensity. A significant Co signal is given, but the overall intensity is quite small. This assumes that some binder is present. Again a C peak is obtained but the intensity is much larger than in spot 1. Partially the signal originates from contamination but some C has to be present, because the acquisition time in both spectra of spot 1 and 2 are the same. Where the oxygen peak originates from could not be figured out.

For the X-ray spectra at spot 3 almost the same result is seen (see figure 4.33). Again a small amount of Co is present. With these two results from the spectra of spot 2 and 3 it can be said that some binder phase is present in the surface region. This would match with the results from previous research about the tribofilm.

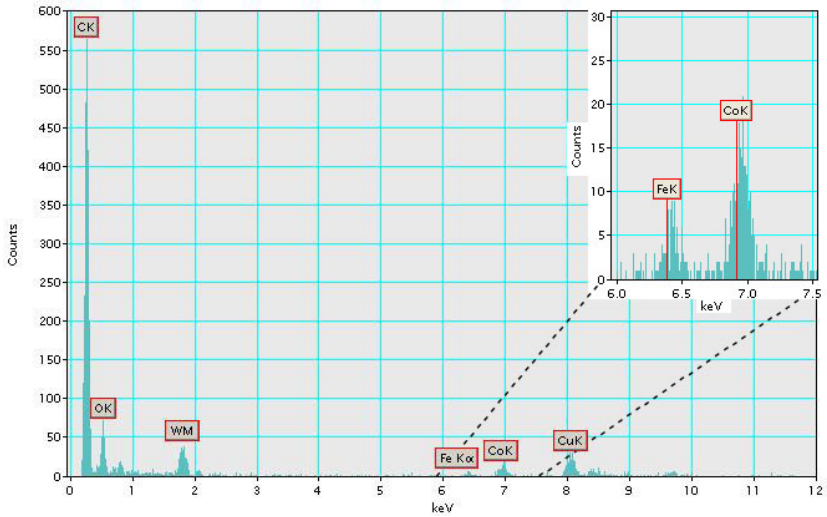

Figure 4.33: STEM-EDX result for spot 3

To specify and make the previous results more reliable EFTEM analyses were made. The EFTEM measurements were performed on the FEI Tecnai F20. In figure 4.34(a) the observed area can be seen. For recording an elemental map the observed area of the

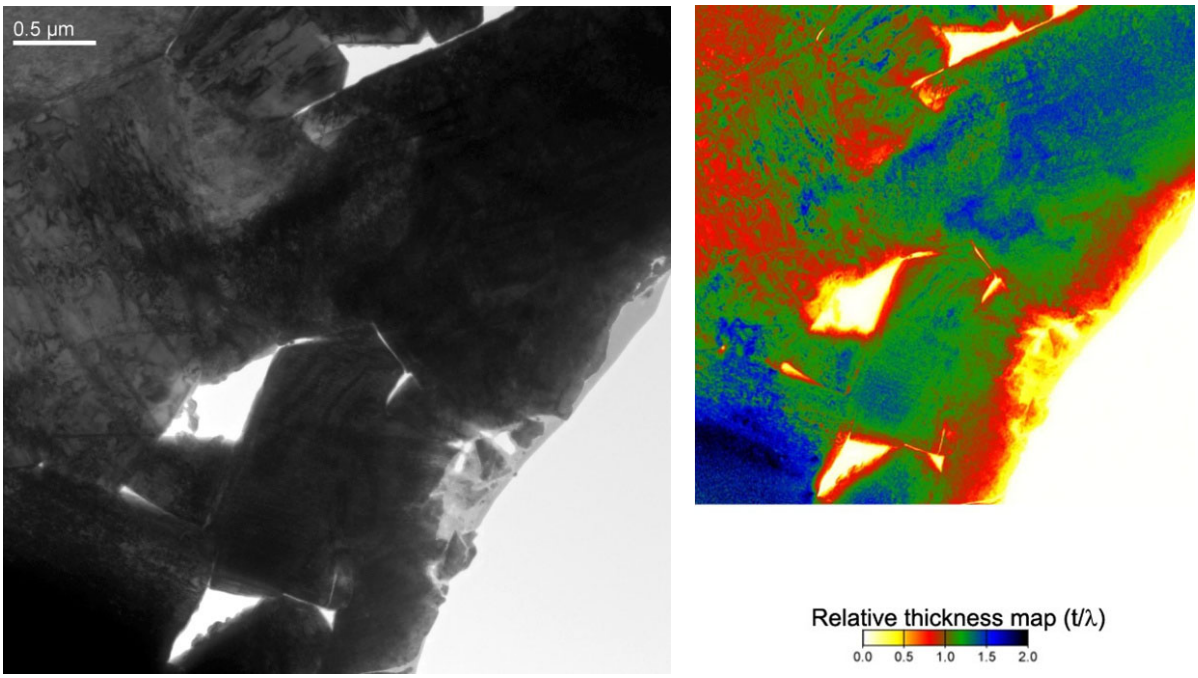

(a) (b)

Figure 4.34: a) TEM BF image of the observed area for EFTEM analysis b) relative thickness map

specimen has to have a limited thickness. The limitation for obtaining elemental maps

is given by the mean free path of the electrons in the given material and should be in the range of $0,5 < t/\lambda < 1,5$ [84]. This circumstance is fulfilled for the surface and a few of the subsurface regions as well for some areas in the bulk (see figure 4.34(b)).

Each element which interacts with the electron beam produces a characteristic change in energy of the scattered electrons. The ionization edges for elements contained in the cemented carbide WC2G can be seen in table 4.4. Both methods (three-window and

Table 4.4: Ionization energies for occuring elements in cemented carbide WC2G

Element	Z	Edge	Ionization energy eV
C	6	K	284
Co	27	$L_{2,3}$	779
W	74	$M_{4,5}$	1809

jump-ratio) were tried (see section 3.1.1). The best results were achieved with the three-window method. In table 4.5 the imaging filter settings for the three-window EFTEM method for C and Co can be seen. Due to the high energy loss of tungsten, no elemental map could be calculated. The recorded images of W showed a too high noise level. For

Table 4.5: Imaging filter settings of EFTEM for the three-window method

Element	Pre-edge window 1 eV	Pre-edge window 2 eV	Post-edge window eV	Slit width eV
C	252,0	272,0	294,0	20,0
Co	721,5	756,5	796,5	35,0

both elements C and Co the acquisition time was $t = 60\,\mathrm{s}$ per window. Because the acquisition time per image is quite long, specimen drift could have happened between the exposures. To avoid artifacts in the elemental maps by spatial drift, a drift correction had to be performed. This drift correction was done with a DigitalMicrograph™ script called statistically determined spatial drift (SDSD) [85]. The obtained drift corrected elemental maps of C and Co can be seen in figure 4.35(a) and 4.35(b).

In the bulk region the binder phase and the tungsten carbide can be distinguished easily. The slight and homogenous distribution of carbon is representing the tungsten carbide (yellow arrows in figure 4.35(a)). At the surface region a lot of carbon can be seen. Considering the previous EDX analysis of the marked region (white arrow) in figure 4.35(a) it can be excluded that the carbon could originate from platinum coverage. Also a contamination due to observations of this area can be excluded, because this would yield to dot-shaped contamination. It looks like that during grinding the surface an enrichment of carbon was taking place at this area.

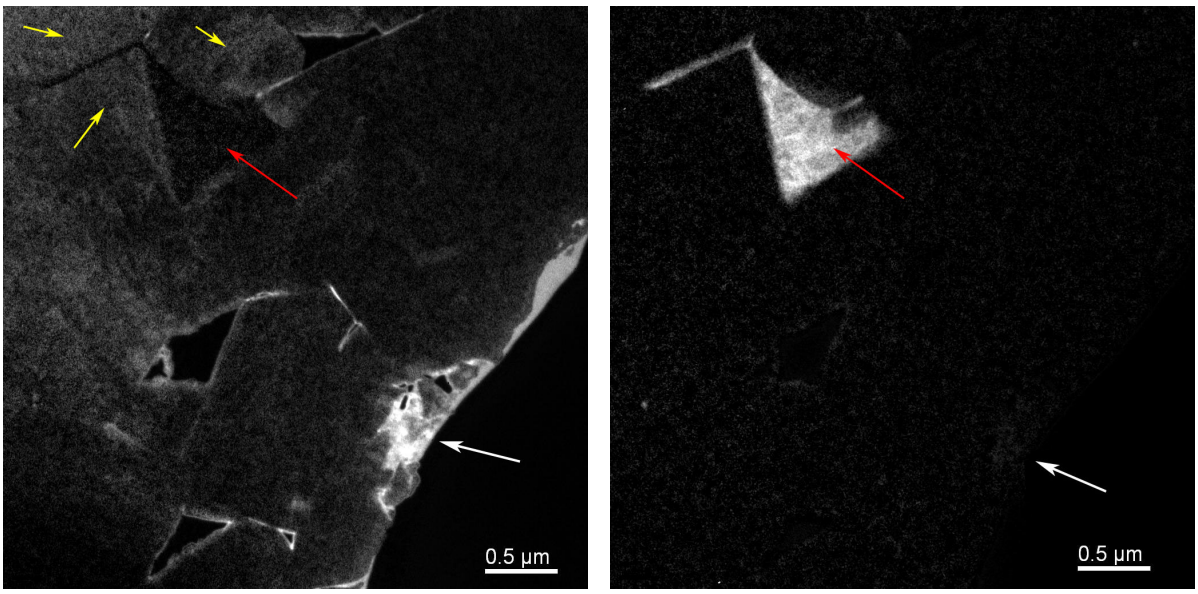

(a) (b)

Figure 4.35: Acquired drift corrected elemental maps of a) carbon and b) cobalt

The brighter regions in the C map at the edges of the WC grains can be attributed to computational artifacts during drift correction. Therefore the alleged higher carbon content at the edges can be neglected.

In the obtained cobalt map just a region in the bulk shows clearly that there is cobalt present (red arrow in figure 4.35(a) and 4.35(b)). Also in the region of interest at the

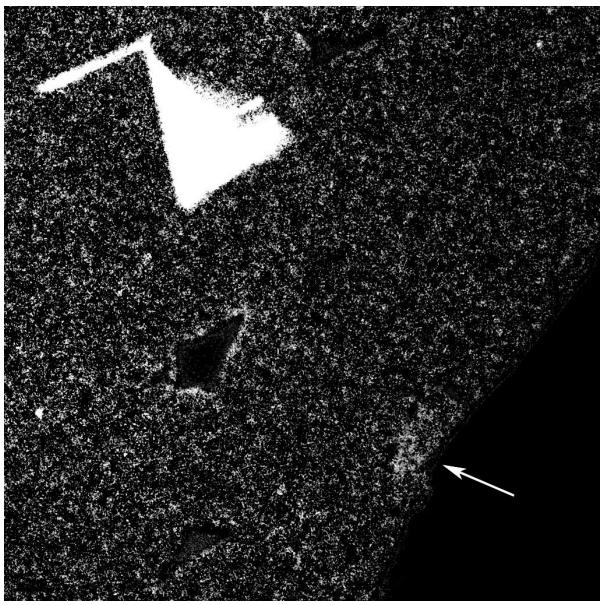

Figure 4.36: Re-adjusted elemental map of Co

surface a slight gathering of cobalt could be assumed (white arrow in figure 4.35(b)). In the rest of the observed area just noise can be seen. To ensure this statement a re-adjustment in DigitalMicrograph™ for the brightness, contrast and gamma control can be done to amplify regions with lower cobalt content. In figure 4.36 the re-adjusted image can be seen. With slight amplifying the slight gathering of Co can be seen better (arrow in figure 4.36). But still the signal is quite weak which indicates a low concentration of cobalt.

Combining the results from EDX and EFTEM it can be assumed that in the surface region some binder phase is left. This would match with the results about tribofilm formation in cemented carbide in previous reserach but here the appearance of the binder is too small.

5 Conclusion

The objective of this master thesis was to figure out why ground indexable inserts may possess a shorter life time in comparison to sinter raw indexable inserts fabricated from the same base material. To achieve this, investigations were made with different microscopes from the macroscopical to the microscopical scale as well as with X-ray diffraction.

The specimens consisted of tungsten carbide with cobalt as binder. Surface and cross section analysis of the cutting tool surfaces of unprocessed and ground tools of base material with two different grain sizes were performed. Four different samples were examined. However, two of them were the same. Therefore, only the results of the coarser grained material WC2 and WC2G are listed here. The main conclusions and observations for the ground specimen are as follows:

- Parts of the tungsten carbide grains are cracked off from the surface and are getting re-embedded. This emerges in SEM and AFM surface analysis as small debris which is mostly located in sinks (see section 4.2.1 and 4.2.2).
- Fracture of the tungsten carbide grains at the surface and subsurface can be identified in SEM and TEM cross-section analysis (see section 4.3.1 and 4.3.2).
- Slip lines appear in the tungsten carbide grains which indicates strain. XRD measurements confirmed an increase of strain of the ground specimen (see section 4.2.3) and slip lines can be seen in SEM cross-section analysis (see section 4.3.1).
- Binder phase extrusion appears up to a depth of about the WC grain size. This can be seen in SEM and TEM cross-section analysis (see section 4.3.1 and 4.3.2).
- The formation of a tribofilm can be assumed with TEM EDX and EFTEM analysis (see section 4.3.2). This film holds together the small debris at the surface.

These observed deformations, especially the fracture of the tungsten carbide grains and binder phase extrusion, cause a brittle surface and subsurface. This may yields a reduced endurance of the ground indexable inserts when compared to the average lifetime of a sinter raw tool.

Bibliography

[1] Sandvik Coromant Deutschland, 5 2008. Available from: `http://www.openpr.de/news/231716/Sandvik-Coromant-zeigt-Produktinnovationen-und-Naehe-zum-Kunden-bei-der-AMB-2008.html`.

[2] Henri Moissan. *Hommage à Henri Moissan, 4 octobre 1931.* Chimie et industrie, Paris, 1932.

[3] H. Tullhoff. *Carbides. Ullmann's Encyclopedia of Industrial Chemistry.* Wiley-VCH Verlag GmbH & Co. KGaA, 2000.

[4] A.T. Santhanam, P. Tierney, and J.L. Hunt. *Metals Handbook, Properties and Selection*, volume 2. AMS International, 1990.

[5] R. Telle. *Structure and Propert of Ceramics*, volume 11, chapter Boride and Carbide Ceramics. VCH, 1994.

[6] David R. Lide, editor. *Handbook of Chemistry and Physics.* CRC Press, 72 edition, 1991.

[7] J.S Schackelford and W. Alexander. *CRC Materials Science and Engineering Handbook.* CRC Press, 2001.

[8] D.N. French and D.A. Thomas. Hardness anisotropy and slip in WC crystals. *Transaction of the AIME*, 233:950–952, 1965.

[9] T. Takahashi and E.J. Freise. Determination of the slip system in single crystals of tungsten monocarbide. *Philosophical Magazine*, 12:1, 1965.

[10] S.B. Luyckx. Slip system of tungsten carbide crystals at room temperature. *Acta Metallurgica*, 18:233–236, 1970.

[11] Siphilisiwe Ndlovu. *The wear properties of tungsten carbide-cobalt hardmetals from the nanoscale up to the macroscopic scale.* PhD thesis, Technische Fakultät der Universität Erlangen-Nürnberg, 2009.

[12] V. Jayaram, R. Sinclair, and D.J. Rowcliffe. Intergranular cracking in WC- 6% Co: an application of the von Mises criterion. *Acta Metall*, 31:373–378, 1983.

[13] B. Roebuck and E. A. Almond. Some observations on indentation tests for hardmetals. In *Recent Advances in Hardmetal Production*, 1979.

[14] S. Bartolucci and H.H. Schlössin. Plastic deformation preceding fracture in tungsten carbide-cobalt alloys. *Acta Metall*, 14:337–339, 1966.

[15] F.R.N. Nabarro and S.B. Luyckx. The theory of strength of tungsten carbide-cobalt compacts. In *International Conference for Strength of Metals and Alloys*, 1968.

[16] Georg Brandt. Dissertatio de semimetallis. *Acta Literaria et Scientiarum Sveciae*, 4:1–10, 1735.

[17] P. Crook. *Metals Handbook*, volume 2. AMS International, 10 edition, 1990.

[18] N.N Greenwood and A. Earnshaw. *Chemie der Elemente*. VCH, 1988.

[19] J. Hinnuber and O. Rudiger. *Cobalt*, 19:57, 1963.

[20] J. Zackrisson, B. Jansson, G.S. Uphadyaya, and H.O. Andrén. WC-Co based cemented carbides with large Cr_3C_2 additions. *International Journal of Refractory Metals & Hard Materials*, 16:417–422, 1998.

[21] A. Horsewell, B. Ralph, and P.R. Howell. An intergranular mechanism for the f.c.c. → h.c.p. martensitic transformation. *Physica status solidi*, 29:587–594, 1975.

[22] S. Mahajan, M.L. Green, and D. Brasen. A model for the f.c.c. → h.c.p. transformation, its applications, and experimental evidence. *Metallurgical and Materials Transactions A*, 8:283–293, 1977.

[23] R.T. Holt. *Cobalt*, 16:145–149, 1972.

[24] V. K. Sarin and T. Johannesson. On the deformation of WC-Co cemented carbides. *Metal Science*, 9:472, 1975.

[25] K. Schröter. Gesinterte harte Metalllegierung und Verfahren zu ihrer Herstellung, 1923.

[26] W. Schatt, K.P. Wieters, and B. Kieback. *Pulvermetallurgie - Technologien und Werkstoffe*. Springer, 2 edition, 2006.

[27] V.K. Sarin. Cemented carbide cutting tools. In D.Y. Chin, editor, *Advances in Powder Technology*. ASM, 1981.

[28] H.C. Lee and J. Gurland. Hardness and deformation of cemented tungsten carbide. *Materials Science and Engineering*, 33:125–133, 1978.

[29] Chang-Soo Kim. *Microstructural-mechanical property relationships in WC-Co composites*. PhD thesis, Carnegie Mellon University, 2004.

[30] H.E. Exner and J. Gurland. A review of parameters influencing some mechanical properties of tungsten carbide cobalt alloys. *Powder Metallurgy*, 13:13–31, 1970.

[31] G.S. Kreimer. *Strenght of hard alloys*. Consultants Bureau, New York, 1968.

[32] Z.F. Zhigang. Correlation of transverse rupture strength of WC-Co with hardness. *International Journal of Refractory Metals & Hard Materials*, 23:119–127, 2005.

[33] S. Amberg and H. Doxner. Porosity in cemented carbides. *Powder Metallurgy*, 20:1–10, 1977.

[34] P. Ettmayer and W. Lengauer. *Encyclopedia of inorganic chemistry*, chapter Carbides: transition metal solid state chemistry. John Wiley & Sons, 1994.

[35] J. Larsen-Basse. Friction in two-body abrasive wear of a WC-Co composite by SiC. *Wear*, 205:231–235, 1997.

[36] H. Klaasen and J. Kübarsepp. Abrasive wear performance of carbide composites. *Wear*, 261:520–526, 2006.

[37] J.Pirso, M. Viljus, K. Juhani, and S. Letunovits. Two-body dry abrasive wear of cermets. *Wear*, 266:21–29, 2009.

[38] M. Antonov and I. Hussainova. Cermets surface transformtaion under erosive and abrasive wear. *Tribology International*, 43:1566–1575, 2010.

[39] I. Hussainova, J. Kübarsepp, and J. Pirso. Mechanical properties and features of cermets. *Wear*, 250:818–826, 2001.

[40] J. Larsen-Basse. Role of microstructure and mechanical properties in abrasion. *Scripta Metallurgica et Materialia*, 24:821–826, 1990.

[41] P.H. Shipway and J.J. Hogg. Dependence of microscale abrasion mechanisms of WC-Co hardmetals on abrasive type. *Wear*, 259:44–51, 2005.

[42] J. Larsen-Basse. Effect of compositen, microstructure and service conditions on the wear of cemented carbide. *Journal of Metals*, 35:35–42, 1983.

[43] K. Jia and T.E. Fischer. Abrasion resistance of nanostructured and conventional cemented carbides. *Wear*, 200:206–214, 1996.

[44] H. Engqvist, S. Ederyd, N. Axén, and S. Hogmark. Grooving wear of singlecrystal tungsten carbide. *Wear*, 230:165–174, 1999.

[45] D.G.F. O-Quigley, S. Luyckx, and M.N. James. An empirical ranking of a wide range of WC-Co grades in terms of their abrasion resistance measured by the ASTM standard B611-85 test. *International Journal of Refractory Metals & Hard Materials*, 15:73–79, 1997.

[46] M.G. Gee. Low load multiple scratch tests of ceramics and hard metals. *Wear*, 250:264–281, 2001.

[47] S. Okamoto, Y. Nakazono, K. Otsuka, Y. Shimoitani, and J. Takada. Mechanical properties of WC-Co cemented carbide with larger WC grain size. *Materials Characterisation*, 55:281–287, 2005.

[48] T. Sailer, M. Herr, H.G. Sockel, R. Schulte, H. Feld, and L.J. Prakash. Microstructural and mechanical properties of ultrafine-grainded hardmetals. *International Journal of Refractory Metals & Hard Materials*, 19:553–559, 2001.

[49] S.G. Bailey and C.M. Perrot. Wear process exhibited by WC-Co rottary cutters in mining. *Wear*, 29:117–128, 1974.

[50] D. Lewis and L.J. Porter. Plastic deformation in tungsten carbide. *Journal of Applied Crystallography*, 2:249, 1969.

[51] Pirso J., Juhani K., Viljus M., and Letunovits S. Two body abrasive wear of WC-Co hardmetals in wet and dry enviroments. In *8th International DAAAM Baltic Conference, Industral Engineering*, 2012.

[52] M. Tournarie. *Comptes Rendus de l'Académie des Sciences*, 242:2016–2164, 1956.

[53] A.J.C. Wilson. *Nature (London)*, 193:568–569, 1962.

[54] J.B.J.W. Hegeman, J.Th.M. De Hosson, and G. de With. Grinding of WC-Co hardmetals. *Wear*, 248:187–196, 2001.

[55] Sabine Neumayer. Wedge polishing as sample preparation method for transmission electron microscopy: A systematic study. Master's thesis, TU-Graz, 2012.

[56] G. Östberg, K. Buss, and M. Christensen. Mechanisms of plastic deformation of WC-Co and Ti(C, N)-WC-Co. *International Journal of Refractory Metals and Hard Materials*, 24:135–144, 2006.

[57] L. S. Sigl and H. E. Exner. Experimental study of the mechanics of fracture in WC-Co alloys. *Metallurgical Transactions A*, 18:1299–1308, 1087.

[58] A.J. Gant and M.G. Gee. Wear of tungsten carbide-cobalt hardmetals and hot isostatically pressed high speed steels under dry abrasive conditions. *Wear*, 251:908–915, 2001.

[59] J. Larsen-Basse, C.M. Perrot, and P.M. Robinson. Abrasive wear of tungsten carbide-cobalt composites. *I Rotary drilling tests, Mater. Sci. Eng.*, 13:83–91, 1974.

[60] J. Larsen-Basse. Binder extrusion of sliding wear of WC-Co alloys. *Wear*, 105:247–256, 1985.

[61] H. Engqvist, H. Högberg, G.A. Botton, S. Ederyd, and N. Axen. Tribofilm formation on cemented carbides in dry sliding conformal contact. *Wear*, 239:219–228, 2000.

[62] M. Herr, T. Sailer, H.G. Sockel, R. Schulte, H. Feld, and L.J. Prakash. Characterisation of wera properties of ultrafine-grainded hardmetals using a special abrasive wheel test. *International Journal of Refractory Metals & Hard Materials*, 19:371–379, 2001.

[63] M. Aristizabal, L.C. Ardila, F. Veiga, M. Arizmendi, J. Fernandez, and J.M. Sanchez. Comparison of the friction and wear behaviour of WC-Ni-Co-Cr and WC-Co hardmetals in contact with steel at high temperatures. *Wear*, 280:15–21, 2012.

[64] Kovametalli-IN Oy, Access 2 2013. Available from: `http://www.kovametalli-in.fi/Pages/Manufacturing.aspx`.

[65] David B. Williams and C. Barry Carter. *Transmission Electron Microscopy.* Springer, second edition, 2009.

[66] Gareth Thomas and Michael J. Goringe. *Transmission Electron Microscopy of Materials.* John Wiley & Sons, Inc., 1979.

[67] M.H. Loretto and R.E. Smallman. *Defect analysis in electron microscopy.* Chapman and Hall, London, 1975.

[68] A. Howie and M.J. Whelan. *Proc. Roy. Soc.*, A 263:217, 1961.

[69] P.B. Hirsch, A . Howie, and M.J. Whelan. *Phil. Trans.*, A 852:499, 1960.

[70] P.Scherrer. *Göttinger Nachrichten Gesell.*, 2:98, 1918.

[71] A.R.Stokes and A.J.C. Wilson. The diffraction of X-rays by distorted crystal aggregates. *Proceedings of the Physical Society London*, 56:174–181, 1944.

[72] G.K. Williamson and W.H. Hall. X-ray broadening from field aluminium and wolfram. *Acta Metallurgica*, 1:22–31, 1953.

[73] Wilson A. J. C., editor. *The Reflexion of X-Rays from the 'Anti-Phase Nuclei' of $AuCu_3$*, volume 181 of *A, Mathematical and Physical Sciences*. Proceedings of the Royal Society of London, 1943.

[74] Jeanne Ayache, Luc Beaunier, Jacqueline Boumendil, Gabrielle Ehret, and Daniele Laub. *Sample preparation handbook for transmission electron microscopy.* Springer, 2010.

[75] Gatan, 4 2010. Available from: `http://www.gatan.com/products/specimen_prep/products/693_Ilion.php`.

[76] L.A. Giannuzzi and F.A. Stevie. A review of focused ion beam milling techniques for tem specimen preparation. *Micron*, 30:197–204, 1999.

[77] Hiroyuki Saito, Akira Iwabuchi, and Tomoharu Shimizu. Effects of Co content and WC grain size on wear of WC cemented carbide. *Wear*, 261:126–132, 2005.

[78] Riccardo Polini, Pierangelo DAntonio, and Enrico Traversa. Diamond nucleation from the gas phase onto cold-worked Co-cemented tungsten carbide. *Diamond and Related Materials*, 12:340–345, 2003.

[79] Riccardo Polini, Fabio Bravi, Fabrizio Casadei, Pierangelo DAntonio, and Enrico Traversa. Effect of substrate grain size and surface treatments on the cutting properties of diamond coated Co-cemented tungsten carbide tools. *Diamond and Related Materials*, 11:726–730, 2002.

[80] Martin Attfield, Paul Barnes, Jeremy Karl Cockcroft, and Huub Driessen. Advanced certificate in powder diffraction on the web. Birkbeck College, London, 2001.

[81] J. Larsen-Basse. Wear of hard metals in rock drilling: a survey of the literature. *Powder Metall*, 16:1–32, 1973.

[82] J. Larsen-Basse, C.M. Shishido, and P.A. Tanouye. Some features of abraded WC-Co surfaces. *Wear*, 19:270–275, 1974.

[83] S.F. Murray and P. Lewis. *Evaluation of rolling contacts in the range of 550°F to 1000°F.* General Electric, Aircraft Nuclear Propulsion Department, 1958.

[84] Egerton R.F, Chen Y.Y, and Yang Y.Y. EELS of „thick“specimens. *Ultramicroscopy*, 38:349–352, 1991.

[85] Bernhard Schaffer, Werner Grogger, and Gerald Kothleitner. Automated spatial drift correction for EFTEM image series. *Ultramicroscopy*, 102:27–26, 2004.